A Review of Turbulence Modelling for use in Sail Flow Analysis

School of Engineering Report No. 603

S. J. Collie*, M. Gerritsen† and P. Jackson‡

Department of Engineering Science
University of Auckland
Private Bag 92019
Auckland
New Zealand

October 23, 2001

Abstract

This document looks at various modern turbulence models and considers their suitability for modelling sail flows. A detailed introduction and analysis of many popular turbulence models is provided. The research being carried out involves modelling the incompressible turbulent flow around sails. Since sails operate in a similar fashion to aerofoils, the general discussion should also apply to other lifting foils.

Our goal is not to develop a universal turbulence model, suitable to all flow situations. The intention of the research is to find a model that is well suited to solving sail flows, while using the minimum computational resources. The focus of the study is on the RANS approach to turbulence modelling. RANS turbulence models have received many successes in the past for aerodynamic applications and are generally less computationally expensive than other modelling options. However RANS models cannot be applied blindly without considering the physics of the application. While a model may perform well in situations that it has been calibrated for, it is likely to do poorly when the physics of the flow regime depart from the conditions the model was designed for.

*Graduate Student, Department of Engineering Science. EMAIL: steve.collie@xtra.co.nz
†Lecturer, Department of Engineering Science
‡Professor, Department of Mechanical Engineering

Contents

1 Turbulence

1.1 Behaviour of Turbulent Flows

Turbulent fluid flows appear regularly in our daily lives. The flow of air into our lungs is turbulent, as is the flow of blood in our hearts. Winds, the sea, the fuels in our cars are all examples of turbulent flows. If you open a tap slightly the water that flows from will be smooth, glassy and reflective. This flow is known as laminar, the particles flow parallel, in cohesion, held side by side by viscosity. If the tap is opened a little further, the flow becomes cloudy. Inside the stream the flow is chaotic, particles jostle, swirling and trading energy. The flow has become turbulent. The same phenomenon can be seen in the smoke streaming upward into still air from a burning cigarette. Immediately above the cigarette, the flow is laminar. A little higher up, it becomes rippled and diffusive [36].

Turbulent flows can be visualised as flows containing eddies: patches of zigzagging, swirling fluid. As eddies jostle about each other they exchange energy. Larger eddies create smaller eddies, which in turn breed even smaller eddies. This cascade of energy continues until the motion of the smallest eddies is dissipated by molecular viscosity, and their kinetic energy is converted to heat.

Laminar flows will often evolve into turbulent flows. The transition to turbulence occurs when the viscous forces of the flow are unable to restrain the non-linear inertial forces. The fluid particles will break their smoothly aligned layered structure and erratic turbulent flow evolves. This phenomenon is known as turbulent transition.

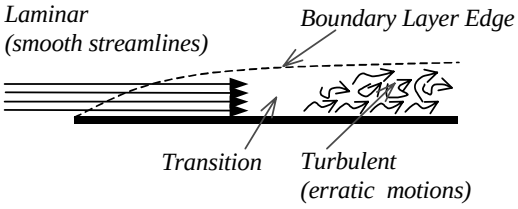

Figure 1: Laminar and turbulent flows.

Turbulent transition was first studied by Osborne Reynolds in 1883 [41]. Reynolds proposed a dimensionless ratio called the Reynolds number as the critical factor for determining whether a flow will be laminar or turbulent. Reynolds first noticed that "the tendency of water to eddy becomes much greater as the temperature rises". It occurred to him that this might be related to the fact that the viscosity of a liquid decreases as the temperature rises. Reynolds performed many experiments observing turbulent transition in a glass walled tank. He released a coloured dye into a laminar flow so that the dye showed a distinct, straight band. As the flow velocity was increased, the dye would suddenly mix with the surrounding fluid. "On viewing the tube by the light of an electric spark, the mass of colour resolved itself into a mass of more or less distinct curls, showing eddies". On increasing the width of the tank, Reynolds found that transition would occur at lower velocities. The ratio of inertial to viscous forces in a fluid flow gives the dimensionless ratio LU/ν, where L and U and the characteristic length and velocity scales of the flow, and ν is the kinematic viscosity of the fluid. On inspection it was clear that transition to turbulence did indeed occur at a critical value of LU/ν. This dimensionless ratio was termed the Reynolds number, Re.

In order for transition to occur there must be a disturbance in the flow. In the case of the Reynolds experiments the shear stress at the wall of the channel instigates non-linear instabilities that subsequently develop turbulence. Turbulent kinetic energy, k, is created by this stress and is passed down through the energy cascade and eventually dissipated to heat at a molecular level. If there is no stress from the mean-flow to provide energy to the turbulent energy cascade then the turbulence in the flow will decay.

If the stress in a flow changes rapidly the production of turbulent kinetic energy, P_k, will not immediately match the dissipation of this energy, ϵ. Such a flow is difficult to model because the length scales over which the turbulence operates are changing in an unpredictable manner. These flows are said to be in turbulent non-equilibrium. Conversely, turbulent equilibrium flows are flows where the production of turbulent kinetic energy matches its dissipation closely so that the scales that turbulence operates upon are neither growing nor decaying.

Turbulent diffusion greatly enhances the transfer of mass, momentum and energy in the flow. Stresses in turbulent flows are orders of magnitude higher than in laminar flows at the same Reynolds number [67].

1.2 Turbulent Boundary Layers

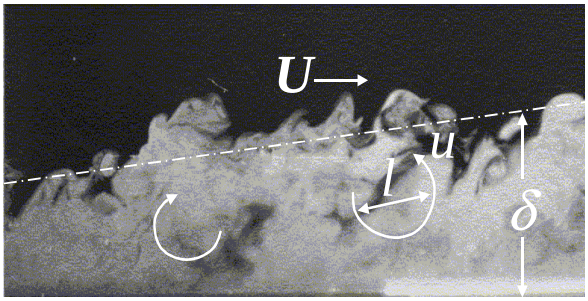

Figure 2: Schematic of large eddies in a turbulent boundary layer. The flow above the boundary layer has a steady velocity U; the eddies move at randomly fluctuating velocities of the order of a tenth of U. The largest eddy size, (l) is comparable to the boundary layer thickness (δ) [67].

Figure 2 shows a schematic of the large-scale motions in a turbulent boundary layer. The size of the largest eddies is limited by the presence of the wall. Typically for boundary layer flows

$$l \simeq \kappa y, \tag{1}$$

where l is the length scale of the turbulent eddies, Von Karman's constant, $\kappa = 0.41$, and y is the distance from the wall. Very close to the wall relation (1) does not hold. Molecular viscosity begins to effect the nature of the turbulent fluctuations, damping the motion of the turbulent eddies.

Experiments have shown that the near-wall region can be divided up into three layers as is depicted in figure 3. In the inner layer, called the viscous sublayer, molecular viscosity plays a

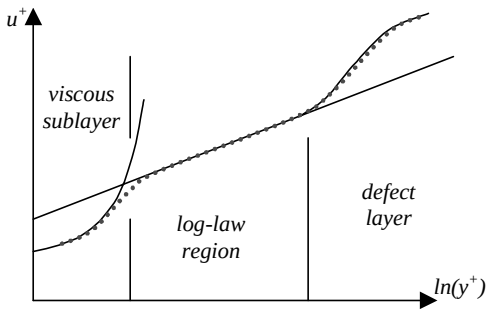

Figure 3: Subdivisions of the near-wall region.

dominant role in momentum transport. Here viscous damping of turbulent fluctuations makes

turbulence modelling difficult. In the outer layer, called the defect layer, turbulence plays the dominant role in momentum transport. In this region molecular viscosity is negligible. Finally, in between these two regions, both turbulence and molecular viscosity play a part in the flow dynamics. In this region, called the log-law region, velocity profiles have been shown to follow a logarithmic profile referred to as the log-law of the wall. The log law of the wall for the tangential velocity is as follows,

$$U^+ \simeq \frac{1}{\kappa} \ln y^+ + B, \tag{2}$$

where U^+ is the dimensionless velocity and y^+ is the normal distance to the wall. These are defined as,

$$U^+ = \frac{u}{u_\tau}, \tag{3}$$

$$y^+ = \frac{u_\tau y}{\nu}, \tag{4}$$

where the friction velocity, $u_\tau = (\tau_w/\rho)^{1/2}$, and τ_w is the shear stress at the wall. Coles and Hirst [10] found estimates of κ and B from correlation with a number of attached, incompressible boundary layer experiments. The values are

$$\kappa = 0.41 \quad \text{and} \quad B = 5.0. \tag{5}$$

The log-law (equation (2)) can be used to describe the flow in the region of $20 < y^+ < 300$ for most simple boundary layer flows, where there are no large pressure gradients. However for more complex adverse pressure gradient flows and separated flows the boundary layer profile in the log-law region has been shown to depart from equation (2) [49, 37, 67].

2 Turbulence Modelling

Turbulence is commonly regarded as the foremost unsolved-problem of classical physics [54]. One of the most notable features of turbulence is the random fluctuation of velocities and pressure through space and time. These fluctuations constitute a wide range of excited length and time scales. Unfortunately for fluid dynamists, these scales extend down to a minute size. The ratio of the largest to smallest eddy sizes is related to the Reynolds number by,

$$\frac{L_{\max}}{L_{\min}} = \mathrm{Re}^{3/4}, \tag{6}$$

where $L_{\max}$ is the size of the largest eddy and $L_{\min}$ is the size of the smallest eddy. As an example, consider a sail with a chord length of 10m in a onset wind-speed of $10\mathrm{m.s}^{-1}$. The Reynolds number for such a flow is approximately 6.8×10^6. The boundary layer thickness can be estimated using, $\delta = L\,\mathrm{Re}^{-1/2}$, giving $\delta \simeq 3.8 \times 10^{-3}$m. By applying equation (1) we find that $L_{\max}$ (using $y = \delta$) in the boundary layer is approximately 0.0016m . Therefore, using equation (6), we discover that the sizes of the smallest eddies are in the order of 1.2×10^{-8}m. Resolving these small eddies would require minute grid sizes. Solving the three-dimensional flow past yacht sails would take thousands of years to solve on the fastest computer available. Therefore turbulence must be modelled.

The scope of turbulence models available today is extensive. However despite almost a century of research in the field of turbulence, there are no successful universal turbulence models. Turbulence modelling can be divided into the following primary fields (ordered in increased computational demand):

1. Reynolds Averaged Navier-Stokes (RANS) modelling, where turbulence is modelled using the Reynolds Averaged Navier Stokes (RANS) equations (equation (10)). The RANS equations are derived by averaging the Navier-Stokes and continuity equations. The core element of RANS modelling is modelling the Reynolds Stresses which describe the effects of the turbulent fluctuations of pressure and velocities. RANS models are the main focus of this document.

2. Large Eddy Simulation (LES), where the large energy containing eddies are computed directly and the effect of the small-scale eddies are modelled using subgrid-scale models [17, 43, 44].

3. Direct Numerical Simulation (DNS), where the full Navier-Stokes equations are solved on grids fine enough, and time-steps small enough to capture the full range of turbulent scales [36].

Only RANS modelling will be considered in this review since the other models are currently too expensive for practical engineering applications. As shown above, DNS requires extremely high grid resolution and is thus unpractical for sail flows. Presently DNS modelling is limited to simple low Reynolds number flows. DNS is predominantly used for generating turbulent flow data for simple problems in order to help develop and validate turbulence models.

LES uses a mathematical model for the small eddies and hence a lower grid resolution is used than for DNS. Typically for non-wall-bounded flows the grid resolution for LES is required to be approximately an order of magnitude lower than if the same simulation was performed using DNS. This is still unpractical for most engineering problems and is certainly unsuitable for sail flows. For wall bounded flows such as sail flows the computational requirements for LES are particularly high since close to the wall even the largest eddies are very small. Hence minute grid spacing in the near-wall region is required when using LES for wall-bounded flows. A new field of research is Detached Eddy Simulation (DES) [57]. In DES a large eddy simulation is used away from walls and the regions close to wall boundaries are resolved using simpler RANS models which do not require the grid resolution in the boundary layer to be as high.

2.1 Reynolds Averaging and the RANS equations

In RANS modelling we break the velocities and pressure down into their mean and fluctuating parts, so that

$$u_i = U_i + u_i', \text{ and } p = P + p'. \tag{7}$$

Here u_i and p are the instantaneous variables we are decomposing, U_i and P are the mean-flow values and u_i' and p' represent the turbulent fluctuations. It is important to note that by "mean-flow" we do not mean a spectral average since U_i and P can still vary through time. More specifically, U_i is the non-turbulent behaviour of u_i. The "mean-flow" variables can be determined using time- or ensemble-averages. Time averaging is used for stationary turbulence where on average the turbulent properties of the flow do not vary with time. The time average, $\overline{f}_T(x)$, of a turbulent property, $f(x,t)$, is defined as,

$$\overline{f}_T(x) = \lim_{T\to\infty} \frac{1}{T} \int_t^{t+T} f(x,t)dt. \tag{8}$$

It is also possible to use a time average when the mean flow is unsteady, so long as the time scale T over which the average is taken is smaller than the important time scales of the mean flow.

Ensemble averaging is used for turbulence where the turbulent properties of the flow vary in both time and space. The ensemble average, $\overline{f_E}(x)$, of a turbulent property, $f(x,t)$, is defined as,

$$\overline{f}_T(x,t) = \lim_{N\to\infty} \frac{1}{N} \sum_{n=1}^{N} f_n(x,t). \tag{9}$$

That is, an average of N identical experiments where $f_n(x,t) = f(x,t)$ in the nth experiment.

Substituting the flow variables in the form given by expression (7) into the incompressible Navier-Stokes equations and taking a time- or ensemble-average yields the Reynolds averaged Navier-Stokes (RANS) equations,

$$\frac{\partial u_i}{\partial x_i} = 0, \tag{10}$$

$$u_j \frac{\partial u_i}{\partial x_j} = -\frac{1}{\rho}\frac{\partial p}{\partial x_i} + \frac{\partial}{\partial x_j}\Big(\nu \frac{\partial u_i}{\partial x_j} - \overline{u_i' u_j'}\Big). \tag{11}$$

where ρ is the density of the fluid and ν is the kinematic viscosity of the fluid. The RANS equations have an almost identical appearance to the instantaneous Navier-Stokes equations. The dependant variables in the RANS equations are now the mean velocities and mean pressure instead of the instantaneous values. The other difference is the appearance of the $-\overline{u_i' u_j'}$ term . This tensor is known as the Reynolds stress tensor, τ_{ij}, which represents the influence of turbulent fluctuations on the mean flow.

When we average the product of two decomposed variables we get

$$\overline{u_i u_j} = \overline{(U_i + u_i')(U_j + u_j')} = \overline{U_i U_j + U_i u_j' + U_j u_i' + u_i u_j} = U_i U_j + \overline{u_i' u_j'}. \tag{12}$$

There is no reason for the product of the fluctuating quantities to have zero mean, i.e. they are correlated. These correlations between the turbulent fluctuations are not measurable by physical experiment. The fundamental problem in turbulence modelling is finding a prescription for computing these unknown correlations.

RANS modelling can be divided into two classes of models: eddy-viscosity models and second order closure models. Eddy-viscosity models approximate the Reynolds-stress tensor as a function of the eddy-viscosity and the mean-stress-tensor, S_{ij}, whereas second order closure models solve modelled differential equations for the Reynolds stresses. Second order closure models will be discussed further in section 8.1.

2.2 The Boussinesq Approximation

The most common approach to eddy-viscosity modelling is known as the Boussinesq approximation. The Boussinesq approximation assumes that the Reynolds-stress-tensor is proportional to the mean-flow stress-tensor, i.e.,

$$\tau_{ij} = \nu_T S_{ij}, \tag{13}$$

where the mean rate-of-strain tensor S_{ij} is given by,

$$S_{ij} = \frac{1}{2}\left(\frac{\partial u_i}{\partial x_j} + \frac{\partial u_j}{\partial x_i}\right). \tag{14}$$

In this relationship the constant of proportionality is the eddy-viscosity, ν_T. It is important to note here that the eddy-viscosity is not a property of the fluid like molecular viscosity, but a property of the flow field and hence will vary throughout the flow domain.

Before the Boussinesq approximation can be applied we need to find a model for the eddy viscosity. The three main types of eddy viscosity models are algebraic (or zero-equation models), one-equation models and two-equation models. Algebraic models use an algebraic specification for the eddy viscosity that is related to mean flow properties, and geometric properties. One-equation models solve a single partial differential equation (PDE) that is used to evaluate the eddy viscosity, whereas two-equation models solve two PDEs. These models will be discussed in the following sections.

The Boussinesq approximation has been criticised as a major limitation of eddy-viscosity models. This is because it assumes that the Reynolds-stress-tensor is isotropic, i.e., its axes align with the mean-stress-tensor. However in many flow situations anisotropy effects can not be

neglected and a full second-order closure is necessary. For anisotropic flows many authors have proposed nonlinear modifications to the Boussinesq approximation [53, 66]. Advanced constitutive relationships for the Reynolds stresses have been derived directly from second order closure models. These models are called Algebraic Stress Models (ASM) [2, 19, 55]. ASM require only slightly more computational effort than models based on the Boussinesq approximation yet in certain flow situations they can provide considerable improvement when the flow is anisotropic. These flow situations include non-equilibrium flows, separated flows and flows with streamline curvature. These flow features all occur for many sail flows. Algebraic Stress Models will be examined further in Section 8.2.

3 Model Overview

The turbulence models that are discussed in this document are listed below. The model types are written in bold and are listed in order of increasing computational demand. There are literally hundreds of turbulence models that exist. This list is merely a selection of a few models that are either relevant to sail flow simulations or have been used for other illustrative purposes.

4 Algebraic Eddy Viscosity Models

4.1 Prandtl's Mixing Length Hypothesis

Prandtl developed the first formation of the eddy viscosity with his mixing-length hypothesis in 1925 [39]. He developed his theory from analogy to molecular transport where molecular viscosity can be described as a product of the fluids thermal velocity, u_{th} and a characteristic length scale known as the mean free path, l_{mfp}, viz,

$$\mu = \frac{1}{2} u_{th} l_{mfp}. \tag{15}$$

Prandtl visualised turbulent flows as flows where particles coalesce into lumps. He replaced l_{mfp} in equation (15) with the mixing length l_{mix}, the distance over which these lumps (eddies) retain

their momentum. He also replaced the thermal velocity with the mixing velocity, u_{mix}, which can be interpreted as the characteristic velocity of the turbulent eddies. Thus the molecular eddy viscosity can be written as,

$$\mu_T = \frac{1}{2}\rho u_{mix} l_{mix}, \tag{16}$$

or in terms of the kinematic eddy viscosity,

$$\nu_T = \frac{1}{2} u_{mix} l_{mix}, \tag{17}$$

since $\mu_T = \rho\nu_T$. Using dimensional analysis Prandtl postulated that the mixing velocity, u_{mix} could be written

$$u_{mix} = \text{constant} \cdot l_{mix} S, \tag{18}$$

where S is the modulus of the mean rate-of-strain tensor, defined as

$$S = \sqrt{2S_{ij}S_{ij}}. \tag{19}$$

Since l_{mix} is not a physical property of the fluid we can absorb the constant in equation (18) and the factor of $1/2$ in equation (16) into the mixing length. Therefore, using equation (13), we can approximate the Reynolds-stress tensor as

$$\tau_{ij} = (l_{mix}^2 S) S_{ij}. \tag{20}$$

To close this model we need to prescribe a method for calculating the mixing length. Prandtl postulated that for flows near solid boundaries the mixing length is proportional to the distance to the nearest boundary such as in equation (1). This makes sense as turbulent eddies are restricted in size by the presence of the wall. For free shear flows the mixing length is approximately proportional to the width of the layer. However the constants of proportionality for these two flows are different. Therefore the mixing length model is incomplete; it requires a new specification of l_{mix} for each new flow.

Two noteworthy algebraic models are the Baldwin-Lomax model [4] and the Cebesi-Smith model [6]. These models are designed and calibrated for boundary layer flows. They are similar in construction and have given similar results for boundary layer flows [67]. However the Cebesi-Smith model requires the boundary layer thickness to be calculated and thus the Baldwin-Lomax model is usually preferred.

4.2 The Baldwin-Lomax Model

The Baldwin-Lomax model is designed specifically for flows where the width of the boundary layer is difficult to determine [4]. This is particularly useful for separated flows where the position of the boundary layer edge is difficult to define. The model divides the domain into two layers, an inner layer and an outer layer. Each layer uses a different algebraic specification for the eddy viscosity. The eddy viscosity is thus defined as

$$\nu_T = \begin{cases} \nu_{T_i}, & y \le y_m \\ \nu_{T_o}, & y > y_m \end{cases}, \tag{21}$$

where y_m is the value of y for which the inner layer eddy viscosity, and the outer eddy viscosity, are of equal value. The eddy viscosities in the inner and outer layers are defined as follows.

Inner Layer:

$$\nu_{T_i} = \ell_{mix}^2 \omega, \tag{22}$$

$$\ell_{mix}^2 = \kappa y \left[1 - e^{-y^+/A_o^+}\right], \tag{23}$$

where ω is the magnitude of the vorticity vector, i.e., $\omega = |\partial U_j/\partial x_i - \partial U_i/\partial x_j|$.

Outer Layer:

$$\nu_{T_o} = \alpha C_{cp} F_{wake} F_{Kleb}(y; y_{\max}/C_{Kleb}), \tag{24}$$

$$F_{wake} = \min\left[y_{\max} F_{\max}; C_{wk} y_{\max} U_{dif}^2/F_{\max}\right], \tag{25}$$

$$F_{Kleb}(y;\delta) = \left[1 + 5.5\left(\frac{y}{\delta}\right)\right]^{-1}, \tag{26}$$

$$U_{dif} = \left(\sqrt{\sum_j U_j^2}\right)_{\max} - \left(\sqrt{\sum_j U_j^2}\right)_{y=y_{\max}}, \tag{27}$$

where $y_{\max}$ is the value of y at which $\ell_{\max}\omega$ achieves its maximum value, and the boundary layer thickness $\delta = y_{\max}/C_{Kleb}$.

The coefficients are:

$$\kappa = 0.40, \quad \alpha = 0.0168, \quad A_o^+ = 26, \quad C_{cp} = 1.6, \quad C_{Kleb} = 0.3, \quad C_{wk} = 1.$$

4.3 Applicability of Algebraic Models

The primary advantage of algebraic models is that they are the easiest models to implement and are computationally the most efficient. However, when using algebraic models one must remember that they are incomplete. That is, they need to be calibrated to each new application and will only work well in situations where they have been fine-tuned. Using an algebraic model blindly, without considering the suitability of the application, is likely to lead to inaccurate results. Although this is sometimes the case even for much more advanced models!

For many years algebraic models were the most commonly used models in the aerodynamics industry. This was due to their computational efficiency. The closure coefficients and expressions were tailored to suit the specific application. Consequently they produced good results for these flows but were unsuitable when the flow situation departed from the ideal.

Wilcox [67] presents results for several boundary layer flows using two of the most popular algebraic models, the Baldwin-Lomax model and the Cebesi-Smith model [6]. The results show that while the models perform well for simple attached flows, they cannot be relied upon for more complicated adverse pressure gradient flows and separated flows. Algebraic models are unsuitable for sail flows since these flows are likely to exhibit considerable amounts of flow separation.

If we could find differential equations for the mixing length and the mixing velocity then we would have a complete model. Then we would be able to compute the eddy viscosity for any flow without knowing any flow information a priori. The first step towards finding such a complete model is one-equation modelling.

5 One-Equation Models

5.1 Traditional One-Equation Models

Traditional one-equation models solve a transport equation for the turbulent kinetic energy per unit mass, k. The turbulent kinetic energy is defined as

$$k = \frac{1}{2}\overline{u_i' u_i'} = \frac{1}{2}\left(\overline{u'^2} + \overline{v'^2} + \overline{w'^2}\right). \tag{28}$$

k describes the kinetic energy of the large-scale eddies, and has dimensions [length]^2/[time]^2, thus the turbulent velocity scale (which is equivalent to Prandtl's mixing velocity) of the flow can be represented as $\sqrt{k}$. The exact equation for k can be obtained by taking the trace of the Reynolds-stress equations, which are defined in section 8.1 (since $\tau_{ii} = -\overline{u_i' u_i'} = -2k$). The exact equation for k is

$$\frac{\partial k}{\partial t} + U_j \frac{\partial k}{\partial x_j} = \tau_{ij} \frac{\partial U_i}{\partial x_j} - \epsilon + \frac{\partial}{\partial x_j} \left[\nu \frac{\partial k}{\partial x_j} - \frac{1}{2} \overline{u_i' u_i' u_j'} - \frac{1}{\rho} \overline{p' u_j'} \right], \tag{29}$$

where the dissipation per unit mass, ϵ, is defined by the correlation

$$\epsilon \equiv \nu \overline{\frac{\partial u_i'}{\partial x_k} \frac{\partial u_i'}{\partial x_k}}. \tag{30}$$

The terms in equation (29) can be interpreted as follows:

$\frac{\partial k}{\partial t} + U_j \frac{\partial k}{\partial x_j}$: The unsteady term and the convective term are collectively known as the **material derivative of** k. This can be described as the rate of change of k along a streamline.

$\frac{\partial k}{\partial t} \tau_{ij} \frac{\partial U_i}{\partial x_j}$: **Production** of k. The rate at which turbulent kinetic energy is generated from the mean flow.

ϵ : **Dissipation** of k. The rate at which turbulent kinetic energy is converted to thermal energy through the action of viscosity. This is also equivalent to the mean rate of work done by the fluctuating part of the strain rate against the fluctuating viscous stresses.

$\frac{\partial}{\partial x_j} \left(\mu \frac{\partial k}{\partial x_j} \right)$: **Molecular Diffusion** of k. The diffusion of k by the fluids natural molecular transport process.

$\frac{\partial}{\partial x_j} \left(\frac{1}{2} \overline{u_i' u_i' u_j'} \right)$: **Turbulent Transport** of k. The rate at which turbulent kinetic energy is transported throughout he fluid by the turbulent fluctuations.

$\frac{\partial}{\partial x_j} \left(\frac{1}{\rho} \overline{p' u_j'} \right)$: **Pressure Diffusion** of k. Turbulent transport of k due to the correlation between velocity fluctuations and pressure fluctuations.

In order to close equation (29) it is necessary to model the unknown correlations of turbulent fluctuations that appear in the turbulent transport and pressure diffusion term. This is achieved using the gradient-diffusion approximation which states that $-\overline{u_j' \phi'} \sim \nu_T \partial \Phi / \partial x_j$. Unfortunately there is no equivalent approximation for the pressure-diffusion term and consequently it has become common-practise to group this these terms together as

$$\frac{1}{2} \overline{u_i' u_i' u_j'} + \frac{1}{\rho} \overline{p' u_j'} = -\frac{\nu_T}{\sigma_k} \frac{\partial k}{\partial x_j}, \tag{31}$$

where σ_k is a closure coefficient calibrated to simple homogeneous flows. Using this approximation the k-equation reduces to

$$\frac{\partial k}{\partial t} + U_i \frac{\partial k}{\partial x_i} = \tau_{ij} \frac{\partial U_i}{\partial x_j} - \epsilon + \frac{\partial}{\partial x_j} \left[(\nu + \nu_T / \sigma_k) \frac{\partial k}{\partial x_j} \right]. \tag{32}$$

In Prandtl's one-equation model [40] ϵ, is determined using

$$\epsilon = \frac{C_\mu k^{3/2}}{\ell_{mix}}, \tag{33}$$

where C_μ is a closure constant equal to 0.09 that was computed through calibration to turbulent shear flows. The Reynolds Stress Tensor, τ_{ij}, is computed using a slightly different form of the Boussinesq approximation given in equation (13),

$$\tau_{ij} = 2\nu_T S_{ij} - \frac{2}{3}k\delta_{ij}. \tag{34}$$

The second term in equation (34) is required to obtain the proper trace of τ_{ij}: For an incompressible flow $S_{ii} = 0$, however from the definition of k, we know that the trace of the Reynolds stress tensor, τ_{ij}, must be equal to $-2k$.

In order to find the eddy viscosity we still need to find the mixing length. Prandtl achieves this in the same fashion as in his algebraic model. Since the mixing length must still be prescribed algebraically the model remains incomplete. There have been many variations on Prandtl's one-equation model, however they all have the limitation that they require an algebraic specification for the mixing length.

5.2 Modern One-Equation Models

A recent trend for one-equation models is to solve a transport equation for the eddy-viscosity, avoiding the use of Prandtl's relationship (equation (16)) between the eddy-viscosity, mixing length and the mixing velocity. Recall that this relationship was drawn from analogy to molecular transport and holds little physical relevance aside from the elegance of dimensional consistency. Models that solve for the eddy viscosity avoid a direct dependence on an algebraic length-scale. However in most cases some form of length scale must still be calculated in order to close the modelled transport equation for the eddy-viscosity. Baldwin and Barth were the first to develop such a model [3]. Their one-equation model was derived from the two-equation standard $k - \epsilon$ model (described in section 6.1) by assuming that the flow is in local equilibrium and neglecting several diffusive terms. Spalart and Allmaras showed that the Baldwin-Barth model becomes ill conditioned and grid-dependent near the edges of free shear layers [52].

The advantage of one-equation models that are based on an equation for the eddy-viscosity is that they do not require the specification of an algebraic length scale, essentially making them complete turbulence models. This makes the models easy to implement and easier to apply to a range of flow situations (however they are still not guaranteed to produce accurate results). They are also easier to use than other one-equation models since they do not require a priori information about the flow situation. Consequentially they are generally the only one-equation models implemented in commercial CFD codes.

Menter formalised a procedure for transforming two-equation models into one-equation eddy-viscosity models [32]. He presents a new model derived from the standard $k - \epsilon$ model which is much more reliable than the Baldwin-Barth model and gives similar results to the parent two-equation model. In several separated and adverse pressure gradient flows the new model significantly outperforms the Standard $k - \epsilon$ model. This improvement is attributed to the use of Bradshaw's assumption for the transport of the Reynolds shear stress, an assumption that has gained much success with other models when used for flows that exhibit adverse pressure gradients [5]. The most popular modern one-equation model is the Spalart-Allmaras model, which is presented below.

5.3 The Spalart-Allmaras Model

Unlike most turbulence models which are calibrated to free shear flows, simple flat plate flows and decaying turbulent flows, Spalart and Allmaras devised their model coefficients and functions from calibration with turbulent flows around aerofoils [52]. The model was built empirically from common production and dissipation terms and includes the diffusive terms that were neglected in the Baldwin-Barth model. Consequently there are no problems near the edges of free shear layers, as were reported for the Baldwin-Barth Model. The Spalart-Allmaras (SA) model is probably

the most popular model for aerodynamic design available today. This model can be written as follows:

Kinematic Eddy Viscosity:

$$\nu_T = \widetilde{\nu} f_{\nu 1}. \tag{35}$$

Eddy Viscosity Equation:

$$\begin{aligned} \frac{\partial \widetilde{\nu}}{\partial t} + U_i \frac{\partial \widetilde{\nu}}{\partial x_i} &= c_{b1} \widetilde{S} \widetilde{\nu} - c_{\omega 1} f_\omega \left(\frac{\widetilde{\nu}}{d} \right)^2 + \frac{1}{\sigma} \frac{\partial}{\partial x_k} \left[(\nu + \widetilde{\nu}) \frac{\partial \widetilde{\nu}}{\partial x_j} \right] \\ &\quad + \frac{c_{b2}}{\sigma} \frac{\partial \widetilde{\nu}}{\partial x_k} \frac{\partial \widetilde{\nu}}{\partial x_k}. \end{aligned} \tag{36}$$

Closure Coefficient and Auxiliary Relations:

$$\begin{gathered} c_{b1} = 0.1355, \quad c_{b2} = 0.622, \quad c_{\nu 1} = 7.1, \quad \sigma = 2/3, \\ c_{w1} = \frac{c_{b1}}{\kappa^2} + \frac{1 + c_{b2}}{\sigma}, \quad c_{w2} = 0.3, \quad c_{w3} = 2, \\ \kappa = 0.41, \quad f_{\nu 1} = \frac{\chi^3}{\chi^3 + c_{\nu 1}^3}, \quad f_{\nu 2} = 1 - \frac{\chi}{1 + \chi f_{\nu 1}}, \quad f_\omega = g \left[\frac{1 + c_{w3}^6}{g^6 + c_{w3}^6} \right]^{1/6}, \\ \chi = \frac{\widetilde{\nu}}{\nu}, \quad g = r + c_{w2} \left(r^6 - r \right), \quad r = \frac{\widetilde{\nu}}{\widetilde{W} \kappa^2 d^2}, \\ \widetilde{W} = W + \frac{\widetilde{\nu}}{\kappa^2 d^2} f_{\nu 2}, \quad W = \sqrt{2 \Omega_{ij} \Omega_{ij}}. \end{gathered} \tag{37}$$

Here $\Omega_{ij} = \frac{1}{2} \left(\partial U_i / \partial x_j - \partial U_j / \partial x_i \right)$ is the mean rotation tensor and d is the distance to the nearest surface.

5.4 Applicability of One-Equation Models

While traditional one-equation models are more sophisticated than algebraic models, they are still incomplete. Therefore care must be taken to ensure that the one-equation model being used is properly calibrated for the particular application. A one-equation model may work well for some types of applications but will fail completely when conditions depart too greatly from what the model is calibrated for. In order to have any confidence in using a model over a range of flows the model must be complete.

Strictly speaking one-equation models based on a transport equation for the eddy-viscosity are complete. Since they solve for the eddy viscosity directly, they do not require a constitutive relation based on two turbulence scales. Such models are much easier to use since they do not need to be recalibrated for each new flow situation.

As an example of the limitation of one-equation models we look at the Spalart-Allmaras model. For attached aerodynamic flows, the Spalart-Allmaras model works better than many more advanced models. However the model gives unacceptable results if used to compute free-shear layers. Even though this model is complete and is designed so that it can be used for any flow without recalibration, it still cannot be relied upon for a range of applications. One-equation models lack the extensiveness and reliability that can be provided (sometimes) if more transport equations are solved.

6 Two-Equation Models

In General, two-equation models solve an equation for the turbulent kinetic energy, k, and one other scale determining transport equation.

6.1 The Standard $k-\epsilon$ Model

The most commonly used two-equation turbulence model over the last three decades is the standard $k-\epsilon$ model [23, 16]. The second transport equation that is solved in the standard $k-\epsilon$ model is for the dissipation of turbulent kinetic energy per unit mass, ϵ. The ϵ-equation is based on the exact equation for ϵ, which is found by taking the following moment of the Navier-Stokes equations,

$$\overline{2\nu\frac{\partial u_i'}{\partial x_j}\frac{\partial}{\partial x_j}\left[N\left(u_i\right)\right]} = 0, \tag{38}$$

where $N(u_i)$ is the Navier-Stokes operator, defined by

$$N(u_i) = \rho\frac{\partial u_i}{\partial t} + \rho u_k\frac{\partial u_i}{\partial x_k} + \frac{\partial p}{\partial x_i} - \mu\frac{\partial^2 u_i}{\partial x_k \partial x_k}. \tag{39}$$

After considerable algebra we obtain the exact equation for ϵ

$$\begin{aligned}\frac{\partial \epsilon}{\partial t} + U_j\frac{\partial \epsilon}{\partial x_j} \quad = \quad & -2\nu\left[\overline{u_{i,j}'u_{j,k}'} + \overline{u_{k,i}'u_{k,j}'}\right]\frac{\partial U_i}{\partial x_j} - 2\nu\overline{u_k'u_{i,j}'}\frac{\partial^2 U_i}{\partial x_j \partial x_k} \\ & -2\nu\overline{u_{i,k}'u_{i,m}'u_{k,m}'} - 2\nu^2\overline{u_{i,km}'u_{i,km}'} \\ & +\frac{\partial}{\partial x_j}\left[\nu\frac{\partial \epsilon}{\partial x_j} - \nu\overline{u_j'u_{i,m}'u_{i,m}'} - 2\frac{\nu}{\rho}\overline{p_{,m}'u_{j,m}'}\right].\end{aligned} \tag{40}$$

This equation is much more complicated than the exact equation for k and involves many new unknown second- and third- order correlations of fluctuating velocities, pressure and velocity gradients. The dissipation of turbulent kinetic energy occurs in the small eddies where the kinetic energy of smallest motions is converted to thermal energy by molecular viscosity. Hence the exact ϵ-equation describes processes of the small eddies yet we use ϵ to determine the eddy-viscosity, which should really be defined by large-eddy scales. Moreover the unknown correlations in equation (40) are approximated using expressions based upon the motions of the large eddies, not the small eddies. Therefore we are really using the modelled ϵ-equation to describe the rate of energy transfer from the large eddies to the small eddies. This is suitable since the rate of dissipation to heat is set by the rate at which energy is handed down the energy cascade. Since we are really modelling the energy transfer in the large eddy-scales it is not surprising that the modelled equation for ϵ bears little relation to its exact equation. Consequently, the poor performance of the $k-\epsilon$ model is often blamed on this transport equation for ϵ. Many researchers have searched for adaptations to the ϵ-equation with little success. However researchers that have used alternative forms for the second transport equation have done much better. The standard $k-\epsilon$ model by Jones and Launder, as described in [23], is as follows:

Eddy Viscosity:

$$\nu_T = C_\mu k^2/\epsilon. \tag{41}$$

Turbulent Kinetic Energy:

$$\frac{\partial k}{\partial t} + U_i\frac{\partial k}{\partial x_i} = \tau_{ij}\frac{\partial U_i}{\partial x_j} - \epsilon + \frac{\partial}{\partial x_j}\left[(\nu + \nu_T/\sigma_k)\frac{\partial k}{\partial x_j}\right]. \tag{42}$$

Dissipation Rate:

$$\frac{\partial \epsilon}{\partial t} + U_i\frac{\partial \epsilon}{\partial x_i} = C_{\epsilon 1}\frac{\epsilon}{k}\tau_{ij}\frac{\partial U_i}{\partial x_j} - C_{\epsilon 2}\frac{\epsilon^2}{k} + \frac{\partial}{\partial x_j}\left[(\nu + \nu_T/\sigma_\epsilon)\frac{\partial \epsilon}{\partial x_j}\right]. \tag{43}$$

Closure Coefficient and Auxiliary Relations:

$$\begin{gathered}C_{\epsilon 1} = 1.44, \quad C_{\epsilon 2} = 1.92, \quad C_\mu = 0.09, \quad \sigma_k = 1.0, \quad \sigma_\epsilon = 1.3, \\ \omega = \epsilon/\left(C_\mu k\right), \quad \ell = C_\mu k^{3/2}/\epsilon.\end{gathered} \tag{44}$$

These closure coefficients are calibrated from comparison to free shear flows and decaying isotropic turbulence.

This model has produced good results for a wide range of simple flows. However, due to its extensive use its deficiencies are well known. The most notable of these is that the standard $k-\epsilon$ model is inaccurate in the vicinity of adverse pressure gradients. In such regions the model overpredicts the turbulent length scale and hence also the eddy viscosity. As a consequence separation is often delayed or prevented completely. For aerodynamic flows in high-lift situations this problem can lead to an over-prediction of lift and an under-prediction of drag, thus exaggerating the performance of aerofoils. The poor performance of the standard $k-\epsilon$ model in adverse pressure gradients is illustrated in sections 10.2 and 10.3. Considering the model's poor performance for adverse pressure gradient flows it is surprising the model is still popular and has not yet been superseded by a more suitable model.

6.2 Low Reynolds Number (LRN) Modifications for the $k-\epsilon$ Model

The standard $k-\epsilon$ model fails to give accurate solutions in the viscous sublayer (i.e., the low-Reynolds number region flow). When near-wall solutions computed using the standard $k-\epsilon$ models are compared to the log-law of the wall (equation (2)) it is evident that the model grossly underpredicts the constant B. Very close to walls, molecular viscosity damps the tangential velocity fluctuations, while normal fluctuations are reduced directly by the wall itself. The standard $k-\epsilon$ model requires modifications to account for the influence of the wall. Many low-Reynolds-number adaptations have been made to the standard $k-\epsilon$ model [8, 16, 23, 26]. It is important to note that these models are not designed specifically for flows at low Reynolds numbers, they are actually models that are designed to account for viscous effects near walls where the local turbulent Reynolds number is low.

LRN $k-\epsilon$ models use viscous damping functions for the closure coefficients in the ϵ-equations, as well as for the eddy-viscosity itself. These damping functions change the values of the closure coefficients in the near wall region. The damping functions are calibrated in order to reproduce the appropriate value of 5.0 for the constant B in the log-law of the wall (equation (2)) and to achieve asymptotic consistency of k, ϵ and the Reynolds-shear-stress in the viscous sublayer region. Effectively, they allow the $k-\epsilon$ model to be integrated through the viscous sublayer. However, they do not improve solutions for adverse pressure gradient flows since it is the defect layer where problems arise for the $k-\epsilon$ model in adverse pressure gradient flows, and in the defect layer these LRN adaptations are negligible.

6.3 The $k-\omega$ Model

In $k-\omega$ models the modelled k-equation is solved together with an equation for the specific rate of dissipation of turbulent kinetic energy, $\omega = \epsilon/k$. Commonly ω is thought of as the characteristic frequency of the turbulent decay process, however more correctly the reciprocal of ω is the time scale on which dissipation of the turbulent energy occurs. Although dissipation occurs at a molecular level, its actual rate is set by the rate of transfer of energy down the eddy spectrum. Hence ω is set by the large-scale motions and therefore it is closely related to mean-flow properties.

The first two-equation model was the $k-\omega$ model of Kolmogorov (1942) [25]. While the Kolmogorov model was a pioneering step in turbulence modelling, his ω-equation possesses several flaws, the most notable being that it does not contain a term to describe the production of ω. Production of ω can be interpreted as the effect that the work of the mean-flow on the turbulent eddies has on the specific dissipation rate.

The most popular $k-\omega$ model is that of Wilcox (1988) [60] which is commonly referred to as the standard $k-\omega$ model:

Eddy Viscosity:

$$\nu_T = \frac{k}{\omega}. \tag{45}$$

Turbulent Kinetic Energy:

$$\frac{\partial k}{\partial t} + U_i \frac{\partial k}{\partial x_i} = \tau_{ij} \frac{\partial U_i}{\partial x_j} - \beta^* k\omega + \frac{\partial}{\partial x_j}\left[(\nu + \sigma^* \nu_T)\frac{\partial k}{\partial x_j}\right]. \tag{46}$$

Specific Dissipation Rate:

$$\frac{\partial \omega}{\partial t} + U_i \frac{\partial \omega}{\partial x_i} = \alpha \frac{\omega}{k} \tau_{ij} \frac{\partial U_i}{\partial x_j} - \beta \omega^2 + \frac{\partial}{\partial x_j}\left[(\nu + \sigma \nu_T)\frac{\partial \omega}{\partial x_j}\right]. \tag{47}$$

Closure Coefficient and Auxiliary Relations:

$$\begin{gathered} \alpha = 13/25, \quad \beta = \beta_o f_\beta, \quad \beta^* = \beta_o^* f_{\beta^*}, \quad \sigma = 1/2, \quad \sigma^* = 1/2, \\ \beta_o = 9/125, \quad f_\beta = 1.0, \quad \beta_o^* = 9/100, \quad f_\beta = 1.0, \\ \epsilon = \beta^* \omega k, \quad \ell = k^{1/2}/\omega. \end{gathered} \tag{48}$$

Unlike the ϵ equation of the standard $k-\epsilon$ model, the ω-equation in the Wilcox $k-\omega$ model was not derived from an exact equation but rather from dimensional analysis and physical reasoning. Wilcox [67] has illustrated that the model not only performs well for free shear flows and flat plate boundary layer flows, but also for more complicated adverse pressure gradient flows and separated flows. This will be demonstrated in sections 10.2 and 10.3. The major downfall of the standard $k-\omega$ model is that it has a large dependence on the freestream boundary condition for ω. In some cases this can lead to inaccurate solutions if ω is not appropriately specified at the freestream boundary. The topic of freestream dependency will be further discussed in sections 6.4 and 6.5 where some solutions to the problem will be given.

6.4 Comparing the $k-\epsilon$ and $k-\omega$ Models

If the modelled ϵ-equation from the standard $k-\epsilon$ model is written in terms of ω then it can be seen that the $k-\epsilon$ and $k-\omega$ models are similar. The ϵ model written in terms of ω is given as follows:

$$\begin{aligned} \frac{\partial \omega}{\partial t} + U_i \frac{\partial \omega}{\partial x_i} &= \alpha \frac{\omega}{k} \tau_{ij} \frac{\partial U_i}{\partial x_j} - \beta \omega^2 + \frac{\partial}{\partial x_j}\left[(\nu + \sigma \nu_T)\frac{\partial \omega}{\partial x_j}\right] \\ &\quad + 2\frac{(\nu + \sigma \nu_T)}{k}\frac{\partial k}{\partial x_j}\frac{\partial \omega}{\partial x_j} + \frac{\omega}{k}\frac{\partial}{\partial x_j}\left[(\sigma - \sigma^*)\nu \frac{\partial k}{\partial x_j}\right] \end{aligned} \tag{49}$$

where $\beta^* = C_\mu$ and α, β, σ and σ^* are simple functions of the $k-\epsilon$ model's closure functions. If, for simplicity, we assume $\sigma = \sigma^*$, then the last term vanishes and the only difference between the $k-\epsilon$ and $k-\omega$ models is the term,

$$2\frac{(\nu + \sigma \nu_T)}{k}\frac{\partial k}{\partial x_j}\frac{\partial \omega}{\partial x_j}. \tag{50}$$

This term is a cross diffusion term and is often written in the form

$$\sigma_d \frac{1}{\omega}\frac{\partial k}{\partial x_j}\frac{\partial \omega}{\partial x_j}, \tag{51}$$

where σ_d is a constant. Cross diffusion does not represent any natural flow process and hence the omission of this term from the $k-\omega$ model cannot be viewed as unphysical. Cross diffusion is merely a term that comes about due to a formal change of variables. Many authors have used

cross diffusion terms to blend between the $k-\epsilon$ and $k-\omega$ models. For example in the next section we will see how Menter uses cross diffusion to create a model that behaves like the $k-\omega$ model close to walls and the $k-\epsilon$ model away from walls. By using cross diffusion away from wall boundaries Menter successfully eliminates the freestream dependency of the $k-\omega$ model.

The standard $k-\omega$ model holds several crucial advantages over the standard $k-\epsilon$ model:

1. It is hard to specify both ϵ and ω at solid boundaries hence there are numerical issues in computing their near-wall derivatives and the specification of boundary conditions. However accurate solutions for ω can still be found when a finite value of ω is specified at the wall. This is not possible for the ϵ-equation as little can be said about the near-wall behaviour of ϵ. The application of these wall boundary conditions will be discussed in more detail in section 9.

2. The ω-equation, as it stands in the standard $k-\omega$ model holds throughout a turbulent boundary layer and provides an accurate prediction of the constant, C, in the low-law of the wall (equation (2)). The ϵ-equation requires modification (viscous damping-functions [16]) for accurate integration through the viscous sublayer.

3. Roughness of a surface can be incorporated using the wall boundary condition for ω. This will be discussed in more detail in section 9.

4. The ω-equation gives a much improved defect-layer solution for flows subject to adverse pressure gradients. The $k-\epsilon$ model over-predicts the turbulent length scale in this region and hence also over-predicts the eddy viscosity. This is the reason for the $k-\epsilon$ models poor prediction of separation points.

5. The ω-equation is not as numerically stiff as the ϵ-equation in the near-wall region. Numerical stiffness makes the ϵ-equation difficult to solve and forces the use of a small time step to account for processes operating over multiple time-scales.

6. In many flow situations the ω-equation is more numerically stable than the ϵ-equation, allowing for larger time-steps.

The first three deficiencies of the ϵ-equation are often treated using various near wall treatments. The most common of these are wall functions, where no computations are performed in the near-wall region and instead the solution is made to asymptote to the log-law of the wall (see section 1.2). Wall functions will be discussed further in section 9.2. Another common approach is to model the near-wall region with a one-equation model that solves for k, thus avoiding solving the ϵ-equation down to the wall. This approach is known as zonal modelling which is discussed further in section 9.3.

6.5 Menter's BSL and SST Models

Wilcox [61] and Menter [29] have shown that the standard $k-\omega$ model possesses an inappropriate dependency on the freestream boundary condition for ω. That is, the value of ω at the far field inappropriately influences the flow throughout the domain. Wilcox [67] has shown that this freestream boundary condition can effect the eddy-viscosity by up to 100%. However the effect is less for boundary layer flows (especially for high Reynolds-number flows) than it is for free-shear flows. Menter has shown that introducing cross diffusion in the form of equation (51) can reduce this dependency[29].

The principle effect of cross diffusion in free-shear flows is to enhance the production of ω, which consequently increases the dissipation of k. In turn this reduces the spreading rates of free-shear layers [67]. Menter introduced cross diffusion in a non-linear manner by multiplying the cross diffusion term with "blending functions" [34, 35]. These functions are zero at the inner edge of a turbulent boundary layer and blend to a unitary value at the outer edge of the layer. Consequently the model behaves like the $k-\epsilon$ model away from walls and the $k-\omega$ model in the

near-wall region. Hence the good boundary layer performance of the Wilcox model is retained while gaining the $k-\epsilon$ model's more stable results for free-shear flows.

Menter presents two new turbulence models based on this zonal approach, the Baseline (BSL) model and the Shear-Stress Transport (SST) model [34, 35]. The BSL model is identical to the standard $k-\omega$ model in the inner 50% of the boundary layer but changes gradually to the $k-\epsilon$ model (in a $k-\omega$ formulation) over the outer half of the layer. The SST model has identical transport equations to the BSL model, but uses a new definition of the eddy-viscosity that is believed to be better at representing the transport of turbulent shear-stress in adverse pressure gradient boundary layers [34]. This new eddy-viscosity relation is based on Bradshaw's assumption that in boundary layer flows the Reynolds shear stress is proportional to the turbulent kinetic energy [5], i.e.,

$$\tau = a_1 k, \tag{52}$$

where $a_1 = 0.3$, and τ is the Reynolds shear stress, i.e., $\tau = \tau_{ij}$, $\forall\ i \neq j$. This relation has been confirmed in a large number of boundary layer experiments [59]. For most two-equation models the relation for the Reynolds stress tensor is given by

$$\tau_{ij} = c_\mu \frac{k^2}{\epsilon} S_{ij} = \frac{k}{\omega} S_{ij}. \tag{53}$$

This can be rewritten to give the Reynolds shear stress,

$$\tau = \sqrt{\frac{\text{Production}_k}{\text{Dissipation}_k}}\, a_1 k, \tag{54}$$

since

$$\text{Production}_k = \tau_{ij} \frac{\partial U_i}{\partial x_j} \simeq \frac{k}{\omega} S_{ij}^2, \tag{55}$$

and

$$\text{Dissipation}_k = \beta^* k\omega = a_1^2 k\omega. \tag{56}$$

For equilibrium boundary layers, production matches dissipation, therefore two-equation models give the turbulent shear-stress equivalent to equation 52. However for adverse pressure gradients the ratio of production to dissipation in the k-equation can be significantly larger than one. There is no experimental evidence that the ratio of $|\tau|/k$ increases to values higher than a_1, therefore equation (53) is unsuitable for adverse pressure gradient flows. Consequently Menter postulated that a more appropriate form for the eddy-viscosity is to use equation (52) in adverse pressure gradients, and the standard relation (equation (53)) otherwise. This lead to the SST expression (equation (58)) in the SST model.

The BSL and SST models are given by

Eddy Viscosity:

$$\text{BSL: } \nu_T = \frac{k}{\omega}. \tag{57}$$

$$\text{SST: } \nu_T = \frac{a_1 k}{\max\left(a_1\omega; SF_2\right)}. \tag{58}$$

Turbulent Kinetic Energy:

$$\frac{\partial k}{\partial t} + U_i \frac{\partial k}{\partial x_i} = \tau_{ij} \frac{\partial U_i}{\partial x_j} - \beta^* k\omega + \frac{\partial}{\partial x_j}\left[(\nu + \sigma^* \nu_T)\frac{\partial k}{\partial x_j}\right]. \tag{59}$$

Specific Dissipation Rate:

$$\frac{\partial \omega}{\partial t} + U_i \frac{\partial \omega}{\partial x_i} = \alpha \frac{\omega}{k} \tau_{ij} \frac{\partial U_i}{\partial x_j} - \beta \omega^2 + \frac{\partial}{\partial x_j} \left[(\nu + \sigma \nu_T) \frac{\partial \omega}{\partial x_j} \right]. \tag{60}$$

Closure Coefficient and Auxiliary Relations:

Let ϕ represent the set of closure constants for the BSL and SST model and let ϕ_1 and ϕ_2 represent the constants from the standard $k-\omega$ and $k-\epsilon$ models respectively.

Set 1, ϕ_1 (standard $k-\omega$):

$$\beta_1 = 0.0750, \quad \beta^* = 0.09, \quad \sigma_{k1} = 0.5, \tag{61}$$

$$\sigma_{\omega 1} = 0.5, \quad \kappa = 0.41, \quad \alpha_1 = \beta_2/\beta^* - \sigma_{\omega 1}\kappa^2/\sqrt{\beta^*}. \tag{62}$$

Set 2, ϕ_2 (standard $k-\epsilon$):

$$\beta_2 = 0.0828, \quad \beta^* = 0.09, \quad \sigma_{k2} = 1.0 \text{ (BSL)}, \quad \sigma_{k2} = 0.85 \text{ (SST)},$$

$$\sigma_{\omega 2} = 0.85, \quad \kappa = 0.41, \quad \alpha_2 = \beta_2/\beta^* - \sigma_{\omega 2}\kappa^2/\sqrt{\beta^*}. \tag{63}$$

In Menter's models the constants ϕ are calculated using the following blend between the constants ϕ_1 $(k-\omega)$ and ϕ_2 $(k-\epsilon)$:

$$\phi = F_1 \phi_1 + (1 - F_1)\phi_2, \tag{64}$$

where

$$F_1 = \tanh\left(\arg_1^4\right), \tag{65}$$

and

$$\arg_1 = \min\left[\max\left(\frac{\sqrt{k}}{0.09\omega y}; \frac{500\nu}{y^2\omega} \right) \frac{4\rho\sigma_{\omega 2} k}{CD_{k\omega} y^2} \right]. \tag{66}$$

Here y is the distance to the nearest surface and $CD_{k\omega}$ is the positive portion of the cross diffusion term, i.e.,

$$CD_{k\omega} = \max\left(2\rho\sigma_{\omega 2} \frac{1}{\omega} \frac{\partial k}{\partial x_j} \frac{\partial \omega}{\partial x_j}; 10^{-20} \right). \tag{67}$$

The blending function for the eddy-viscosity relation in the SST model is defined,

$$F_2 = \tanh\left(\arg_2^2\right), \tag{68}$$

where

$$\arg_2 = \max\left(2\frac{\sqrt{k}}{0.09\omega y}; \frac{500\nu}{y^2\omega} \right). \tag{69}$$

These blending functions have been derived through calibration with free-shear and boundary layer flows. Compared with the standard $k-\omega$ model, the BSL and SST models have been shown to have considerably decreased dependency on freestream boundary conditions [31, 34, 35]. The SST model in particular has gained good results for flows involving adverse pressure gradients and separation [31, 34, 35]. This is due to the modified eddy-viscosity relation (equation (58)), which is the primary difference between the models.

Parameters	$k-\omega$ **1988**	$k-\omega$ **1998**
α	5/9	13/25
β	$\beta_o f_\beta$	$\beta_o f_\beta$
β^*	$\beta_o^* f_{\beta^*}$	$\beta_o^* f_{\beta^*}$
β_o	3/40	9/125
β_o^*	9/100	9/100
f_β	1.0	$\frac{1+70\chi_\omega}{1+80\chi_\omega}$
f_{β^*}	1.0	$\begin{cases} 1.0, & \chi_k \leq 0 \\ \frac{1+680\chi_k^2}{1+400\chi_k^2}, & \chi_k > 0 \end{cases}$

Table 1: Closure parameters for the 1988 and 1998 $k-\omega$ models.

6.6 The $k-\omega$ 1998 Model

In [67] Wilcox presents a new $k-\omega$ model that improves upon the standard $k-\omega$ model's accuracy for free-shear flows. This $k-\omega$ model includes new coefficients for the dissipation terms in the k- and ω-equations. The changes to the 1988 model are summarised in table 1.
In table 1

$$\chi_\omega = \left| \frac{\Omega_{ij}\Omega_{jk}S_{ki}}{(\beta_o^*\omega)^3} \right|, \tag{70}$$

$$\chi_k = \frac{1}{\omega^3}\frac{\partial k}{\partial x_j}\frac{\partial \omega}{\partial x_j}, \tag{71}$$

and Ω_{ij} is the mean-rotation tensor defined by

$$\Omega_{ij} = \frac{1}{2}\left(\frac{\partial U_i}{\partial x_j} - \frac{\partial U_j}{\partial x_i}\right). \tag{72}$$

The new closure in the ω-equation (i.e., equation (70)) only influences three-dimensional flows. This addition to the model provides improvement in the spreading rates for round and radial jets (see table 2). The new closure in the k-equation (i.e., equation (71)) successfully reduces the model's dependency on the freestream boundary condition for ω. The new closure coefficient is a function of χ_k, a dimensionless version of the cross diffusion term. It has no influence in the boundary layer, but enhances dissipation in free shear flows, reducing the predicted spreading rates. Both closures have been calibrated to provide spreading rates consistent with measurements for far wakes, mixing layers, and plane, round and radial jets.

As previously mentioned, the standard approach to removing freestream dependency is to add cross diffusion in the ω-equation in order to the increase dissipation of k. This approach makes the model behave like the standard $k-\epsilon$ model in free-stream regions of the flow. Wilcox prefers to control the dissipation of k directly, using the closure function for the production term in the k-equation. By observing this closure function, it can be seen that the cross diffusion parameter is only used when it is positive. This is done so that the standard $k-\omega$ model is retained in the viscous sublayer, where it performed admirably.

Wilcox tested the $k-\omega$ (1998) model on free-shear flows and in a perturbation analysis of the boundary layer [67]. In the latter case results are almost identical to the standard $k-\omega$ model. Table 2 presents the calculated and measured spreading rates for free-shear test cases. Of the three models presented, the $k-\omega$ (1998) model provides the best results. The spreading rates for the standard $k-\omega$ model are higher than the measured data. However Wilcox has shown that free-shear results for the standard $k-\omega$ model depend on the freestream boundary conditions. Accurate spreading rates are predicted if different boundary conditions are used

Flow	$k-\omega$ **(98)**	$k-\omega$ **(88)**	$k-\epsilon$	**Measured**
Far Wake	0.339	0.496	0.256	0.365
Mixing Layer	0.105	0.141	0.098	0.115
Plane Jet	0.101	0.135	0.146	0.100-0.110
Round Jet	0.088	0.369	0.185	0.860-0.960
Radial Jet	0.099	0.317	0.110	0.096-0.110

Table 2: Free-shear flow spreading rates [11].

for each flow [62]. However Wilcox could not find any obvious physical reason for selecting each boundary condition. This illustrates the problem of freestream dependency: for most engineering applications the correct value of ω at boundary is unknown or at best imprecise and therefore it is difficult to get trustworthy results.

Table 2 presents an interesting anomaly; both the $k-\omega$ (1988) model and the $k-\epsilon$ model predict greater spreading rates for the round jet than the plane jet. However, experiments indicate that the opposite occurs with the round-jet spreading rate being about 10% lower than that of the plane jet. This is known as the round-jet/plane-jet anomaly. The $k-\omega$ (1998) model and the Robinson, Harris and Hassan enstrophy-equation model [42] are the only RANS models that correctly predict this trend. The Robinson et al. model uses the standard model equation for k and a new transport equation for the enstrophy ζ, also known as the vorticity variance, ω^2. The model is calibrated using round-jet free-shear flow and the decay of homogeneous turbulence. This model preforms well for free-shear flows (for which it was designed), however its use is not recommended for boundary layer flows.

In a perturbation analysis of the boundary layer Wilcox [67] investigates the freestream sensitivity of the $k-\omega$ (1998) model by varying the freestream value of ω. It is found that the skin-friction coefficient varies by just 3% when ω_∞ is varied by several orders of magnitude. Results for the standard $k-\omega$ model were not reported.

Wilcox's $k-\omega$ (1998) model produces good results for adverse pressure gradient flows, however no results are presented for separated flows. Wilcox [67] claims that results for separated flows are likely to be similar to the standard $k-\omega$ model, which performed well.

Peng, Davidson and Holmberg introduced a modified $k-\omega$ model for recirculating flows [38]. They claim that the standard $k-\omega$ model over-predicts the reattachment length for a backward facing step flow with large expansion ratio ($H/h = 6$). They include a cross diffusion term in the ω-equation and re-establish the closure coefficients and damping functions. Unlike the cross diffusion models of Menter, this cross diffusion term is active in both the near-wall and far-wall regions. In the near-wall region it increases the production of k, which has the consequence of reducing the reattachment length for recirculating flows. It was found that the modified model provided a more accurate prediction of the reattachment length for the large expansion backward facing step flow (5% higher c.f. 35% higher). It was also found that for a low expansion ratio step ($H/h = 1.2$) the modified model also improved upon the Wilcox model, particularly for turbulence kinetic energy profiles downstream of the step. However despite getting good results for these difficult test cases the model still should not be relied upon since recirculating flows by themselves are an incomplete test for turbulence models. Wilcox investigates this modified $k-\omega$ model for free-shear flows [67]. Results showed that the model performs poorly compared with both the standard $k-\omega$ model and the standard $k-\epsilon$ model. Peng et al.'s model is an example of how good results are obtainable when a model is tailored for a specific flow, but also how a model designed in this fashion is unlikely to be suitable for a universal range of flows.

Arguably, one of the shortcomings of the $k-\omega$ model is that it gives incorrect asymptotic solutions for the turbulent kinetic energy near solid surfaces [60]. These asymptotic solutions are based on a Taylor's series expansion and are hence only valid in the immediate vicinity of the wall. However we must question how important retaining asymptotic behaviour is since molecular viscosity largely outweighs eddy-viscosity in this region. Furthermore, it is known that the $k-\omega$ model produces excellent solutions for the viscous sublayer and the log-layer. However

in search for mathematical correctness, many authors have attempted to gain accurate near wall asymptotic behaviour. An example of this is Speziale's $k-\tau$ model.

6.7 The $k-\tau$ Model

Speziale, Abid and Anderson [56] have derived a two-equation model that solves for the turbulent kinetic energy and τ, the time scale at which dissipation of turbulent kinetic energy occurs. This $k-\tau$ model is calibrated to give excellent asymptotic behaviour for all variables in the near wall region. The use of τ as the second variable has the advantage that τ vanishes at solid boundaries. As will be shown in section 9, ω and ϵ cannot be appropriately defined at walls and hence specification of boundary conditions is difficult and numerical issues arise in the evaluation of derivatives near the surface.

The modelled equation for τ is based on the exact equation for τ, which has been derived in a similar fashion to the exact equation for ϵ [56]. The modelled τ equation of the $k-\tau$ model [56] is given by,

$$\begin{aligned}\frac{\partial \tau}{\partial t}+U_i\frac{\partial \tau}{\partial x_i} &= (1-C_{\epsilon 1})\frac{\tau}{k}\tau_{ij}\frac{\partial U_i}{\partial x_j}-\beta\left(C_{\epsilon 2}-1\right)+\frac{2}{k}\left(\nu+\frac{\nu_T}{\sigma_{\tau 1}}\right)\frac{\partial k}{\partial x_i}\frac{\partial \tau}{\partial x_i}\\ &\quad -\frac{2}{\tau}\left(\nu+\frac{\nu_T}{\sigma_{\tau 2}}\right)\frac{\partial \tau}{\partial x_i}\frac{\partial \tau}{\partial x_i}+\frac{\partial}{\partial x_j}\left[\left(\nu+\sigma\nu_T\right)\frac{\partial \tau}{\partial x_j}\right], \end{aligned} \tag{73}$$

where

$$\begin{aligned} &C_{\epsilon 1}=1.44, \quad C_{\epsilon 2}=1.83\left(1-f_1\right), \quad f_1=\frac{2}{9}e^{-\mathrm{Re}_t^2/36},\\ &\mathrm{Re}_t=\frac{k^2}{\nu\epsilon}, \quad f_2=\left[1-e^{-y^+/4.9}\right]^2, \quad \sigma_{\tau 1}=\sigma_{\tau 2}=1.36. \end{aligned} \tag{74}$$

These closures are calibrated using flat plate boundary layer flows and special attention is paid to ensure assymtotic consistency of all flow variables. As with LRN $k-\epsilon$ models, the $k-\tau$ requires damping of the eddy-viscosity in the near-wall region to account for the effects of solid surfaces and molecular viscosity. The damped equation for the eddy-viscosity is computed using,

$$\nu_T=C_\mu f_\mu k\tau \tag{75}$$

where

$$f_\mu=\left(1+\frac{3.45}{\sqrt{\mathrm{Re}_t}}\right)\tanh\left(\frac{y^+}{70}\right) \tag{76}$$

When the τ-equation is rewritten in terms of ϵ, the resulting equation is almost identical to the ϵ-equation of the $k-\epsilon$ models. The only differences are in the closure functions and constants. If the τ-equation is written in terms of ω then we get

$$\begin{aligned}\frac{\partial \omega}{\partial t}+U_i\frac{\partial \omega}{\partial x_i} &= \alpha\frac{\omega}{k}\tau_{ij}\frac{\partial U_i}{\partial x_j}-\left(C_{\epsilon 1}f_2-1\right)\omega^2\\ &\quad \frac{2}{k}\left(\nu+\frac{\nu_T}{\sigma_1}\right)\frac{\partial k}{\partial x_j}\frac{\partial \omega}{\partial x_j}+\frac{\partial}{\partial x_j}\left[\left(\nu+\frac{\nu_T}{\sigma_{\tau 2}}\right)\frac{\partial \omega}{\partial x_j}\right]. \end{aligned} \tag{77}$$

This equation differs from Wilcox's ω-equation by the presence of cross diffusion and by the damping of the ω^2 dissipation term. The cross diffusion term can be broken into two parts,

$$\frac{2\nu}{k}\frac{\partial k}{\partial x_j}\frac{\partial \omega}{\partial x_j}, \quad \text{and} \quad \frac{2\nu_T}{\sigma_{\tau 1}k}\frac{\partial k}{\partial x_j}\frac{\partial \omega}{\partial x_j}\equiv\frac{2}{\sigma_{\tau 1}}\frac{1}{\omega}\frac{\partial k}{\partial x_j}\frac{\partial \omega}{\partial x_j} \tag{78}$$

Speziale et al. show that the first term appears in the exact equation for ω and that its inclusion leads to correct asymptotic solutions for k approaching solid boundaries. This first cross diffusion term has also been used by Peng et al. [38]. The second cross diffusion term is of the same form as that used by Menter for removing the freestream dependency of the $k-\omega$ model [29, 34, 35]. While the $k-\tau$ model holds attractive advantages for near-wall modelling, it retains the deficiencies of the $k-\epsilon$ model for adverse pressure gradient flows.

6.8 Other Two-Equation Models

In recent years there have been several new two-equation $k-\epsilon$ models based upon the deficiencies of the standard $k-\epsilon$ model for adverse pressure gradient flows. The RNG $k-\epsilon$ model and the Realizable $k-\epsilon$ model were both studied by the author in [11, 12].

The RNG $k-\epsilon$ model was derived from Renormalization Group Theory by Yakhot and Orszag [68]. This model has been shown to improve upon the standard $k-\epsilon$ model for some adverse pressure gradients and separated flows. However for free shear flows the results are poorer that the $k-\epsilon$ model. Predicted and measured spreading rates are an average of 29% different for the RNG $k-\epsilon$ model and 18% for the standard $k-\epsilon$ model [67]. The RNG $k-\epsilon$ model also includes a correction term in the ϵ-equation that improves predictions for flows with large streamline curvature.

Lumley [28] showed that in situations of high mean strain rates, the Reynolds stresses may become unphysical . The realizable $k-\epsilon$ model of Shih et al. obeys certain mathematical restraints on the Reynolds stresses consistent with the physics of turbulent flows [50]. In the standard $k-\epsilon$ model the diagonal components of the tensor may become negative if the mean strain rate is large. However by definition k is a positive quantity and so we require $\overline{u_i'^2} \geq 0$ for a realizable model. The second realizability restraint is that the Schwartz inequality is preserved for the Reynolds stress tensor. That is,

$$\overline{u_i'u_j'} \leq \sqrt{\overline{u_i'^2 u_j'^2}}, \quad \forall i,j. \tag{79}$$

In order in maintain relaizable Rynolds stresses the realizable $k-\epsilon$ model uses a varaible form for the coefficient C_μ in equation (41).

In [11] and [12] the performances of the standard $k-\epsilon$, RNG $k-\epsilon$ and the realizable $k-\epsilon$ models with both wall functions and a zonal model were compared for the turbulent flow over a backward facing step (see section 9.2 for details on wall functions and zonal models). The results for the reattachment lengths of the recirculation region are given in table 3. The realizable $k-\epsilon$

Non–equilibrium wall functions	
Turbulence model	*Reattachment Length*
standard $k-\epsilon$	$5.9h$
RNG $k-\epsilon$	$6.7h$
realizable $k-\epsilon$	$7.0h$
Experimental Data	$8.0h$
Zonal model	
Turbulence model	*Reattachment Length*
standard $k-\epsilon$	$4.2h$
RNG $k-\epsilon$	$7.1h$
realizable $k-\epsilon$	$7.8h$

Table 3: Reattachment lengths for the different turbulence models.

model predicts the reattachment length closest to the experimental data. It was found that this model resolved the recirculation region more accurately that the others and consequently the realizable $k-\epsilon$ model was chosen for the three-dimensional sail computations performed in [11] and [12]. When the models were used to compute the flow around two-dimensional sails at low angles of attack, with no separation, the models all gave identical results.

Unfortunately, like the standard $k-\epsilon$ model, the RNG and realizable $k-\epsilon$ models cannot be integrated through the viscous sublayer without modification. Moreover, while they improve on the standard $k-\epsilon$ model for adverse pressure gradients and separated flows, the results are still poor and better backward facing step results have been achieved with $k-\omega$ based models. Therefore the RNG $k-\epsilon$ and the realizable $k-\epsilon$ will be dismissed in favour of other more suitable models such as the $k-\omega$ (1998) model and the SST model.

Several two equation models have been developed for transitional flows. Examples of these are the $k-\epsilon$ variant of Abid [1] and the $k-\omega$ transition model developed by Wilcox [**?**]. Transition models will be discussed further in section 10.6.

6.9 Summary of Two-Equation Models

Two-equation models provide an attractive blend between simplicity and accuracy. They are the simplest complete models that can be applied to a full range of different flow types. Since there is no immediate requirement for specification of turbulent length scales or calibration of algebraic functions it is easy to apply two-equation models without considering the suitability of the application. However this may be a mistake. Most two-equation models have been designed with a particular application in mind. Consequently they often work well for applications they are calibrated for but are just as likely to present unsuitable results for extraneous applications.

The standard $k-\epsilon$ model has been calibrated using simple flows such as decaying homogeneous turbulence and flat plate flow. Consequently it performs well for a wide range of simple flows. However care must be taken when using the model for more difficult flows, especially flows that exhibit adverse pressure gradients and separation regions.

The standard $k-\omega$ model has the advantage that it can be integrated through boundary layers without modifications being made to the model. It also performs well for adverse pressure gradients. However the model is unsuitable for free shear flows when the correct freestream boundary condition for ω is uncertain. In fact, care must be taken when using freestream boundary conditions with this model for all flows.

The $k-\omega$ 1998 model contains a modification to the dissipation term in the k-equation that significantly reduces this freestream dependency. Consequently the new model produces excellent results for free shear flows. In the author's opinion, this model is the most suitable eddy-viscosity model for use with a wide range of flow types. However as for most other models the $k-\omega$ 1998 model still has some difficulty with many separated flows and flows with large streamline curvature.

Menter's BSL and SST avoid the standard $k-\omega$ model's problems with freestream dependency by blending from the $k-\omega$ model near walls into the $k-\epsilon$ model outside the boundary layer. These models perform well for wall bounded flows while retaining the $k-\epsilon$ model's average performance for free shear flows. The SST model is designed for adverse pressure gradients and separated flows and consequently performs well for these difficult flows. Away from these regions the SST model performs identically to the BSL model and therefore the model can also be used in a wide range of flow situations.

The $k-\tau$ model has the attractive advantages of a vanishing wall boundary condition for τ and provides excellent asymptotic consistency of the turbulence parameters at solid boundaries. However the model retains many of the deficiencies of the $k-\epsilon$ model and performs poorly for adverse pressure gradients.

There are numerous other two-equation models that have been developed. The models presented in this section are the most popular models have generally been tested thoroughly. Most other models are variants on the presented models and in most cases only exhibit subtle differences.

7 Other Models

7.1 The Half-equation Model

The so called half-equation Johnson-King model is an adaptation of the Cebeci-Smith [6] algebraic model. This model was first devised by Johnson and King [22] in 1985, and later revised by Johnson and Coakley [21] in 1990. The model solves a single ordinary differential equation (ODE) for the maximum Reynolds shear stress in the boundary layer. The half-equation terminology comes about since the model is more comprehensive than algebraic models, yet not as advanced as one-equation models. The Johnson-King model:

Eddy Viscosity:

$$\mu_T = \mu_{T_o} \tanh\left(\frac{\mu_{T_i}}{\mu_{T_o}}\right). \tag{80}$$

Inner Layer:

$$\mu_{T_i} = \rho\left[1 - \exp\left(-\frac{u_D y/\nu}{A^+}\right)\right]^2 \kappa u_s y, \tag{81}$$

$$\sqrt{\rho}u_s = (1-\gamma_2)\sqrt{\tau_w} + \gamma_2\sqrt{\tau_m}, \tag{82}$$

$$\gamma_2 = \tanh\left(y/L_c\right), \tag{83}$$

$$L_c = \frac{\sqrt{\tau_w}}{\sqrt{\tau_w}+\sqrt{\tau_m}} L_m, \tag{84}$$

$$L_m = \begin{cases} \kappa y_m, & y_m/\delta \le C_1/\kappa \\ C_1\delta, & y_m/\delta > C_1/\kappa \end{cases}, \tag{85}$$

$$u_m = \sqrt{\tau_m/\rho_m}, \tag{86}$$

$$u_D = \max\left[u_m, u_\tau\right], \tag{87}$$

where the subscript m denotes the value at $y = y_m$, where the Reynolds shear stress is at its maximum value, $\tau_m = (\rho\tau_{xy})_{\max}$. Additionally u_τ is the friction velocity and ρ_w is the density at the surface. The velocity scales u_s and u_D were included by Johnson and Coakley [21] to improve predictions for reattaching flows and flows with non-trivial compressibility effects.

Outer Layer:

$$\mu_{T_o} = \alpha\rho U_e \delta_v^* F_{Kleb}\left(y;\delta\right)\sigma\left(x\right), \tag{88}$$

where F_{Kleb} is the Klebanoff intermittency function given by equation (26), U_e is the boundary-layer edge velocity and δ_v^* is the velocity thickness defined by

$$\delta_v^* = \int_0^\delta \left(1 - U/U_e\right) dy. \tag{89}$$

The $\sigma\left(x\right)$ function is the "non-equilibrium" parameter which is controlled by the following ODE for the maximum Reynolds shear stress in terms of $u_m = \sqrt{\tau_m/\rho_m}$,

$$U_m \frac{d}{dx}\left(u_m^2\right) = a_1\left[\frac{(u_m)_{eq} - u_m}{L_m}\right] u_m^2 - C_{dif}\left[\frac{u_m^3}{C_2\delta - y_m}\right]\left|1 - \sigma^{1/2}\left(x\right)\right|, \tag{90}$$

where U_m is the mean velocity and $(u_m)_{eq}$ is the value of u_m according to the "equilibrium" algebraic model $[\sigma\left(x\right) = 1]$. Equation (90) is solved along with the RANS equations to determine τ_m. As the solution proceeds the coefficient $\sigma\left(x\right)$ in equation (88) is altered to ensure,

$$\tau_m = \left(\mu_T\right)_m \left(\frac{\partial U}{\partial y} + \frac{\partial V}{\partial x}\right)_m. \tag{91}$$

That is, the eddy viscosity profile is adjusted to agree with the calculated maximum Reynolds shear stress, τ_m.

Closure Coefficients:

$$\begin{aligned} \kappa &= 0.40, \quad \alpha = 0.0168, \quad A^+ = 17, \\ \alpha_1 &= 0.25, \quad C_1 = 0.09, \quad C_2 = 0.70, \\ C_{dif} &= 0.50, \quad \text{for } \sigma(x) \geq 1, \quad 0 \text{ otherwise.} \end{aligned} \tag{92}$$

The Johnson-King model is designed to account for departures from equilibrium by adjusting the eddy viscosity profile so that the ODE for the maximum Reynolds shear stress is satisfied. This equation for the maximum Reynolds shear stress is based upon Bradshaws assumption (equation (52)) and thus the model is tailored for adverse pressure gradient flows which are commonly in non-equilibrium. For equilibrium flows the model should perform very similarly to the Cebeci-Smith algebraic model [6], upon which it is based. The Johnson-King model has received good results for many adverse-pressure gradient flows and separating and reattaching flows. Results for such flows will be presented in section 10.3. The downside of the model is that it is complicated compared with the Cebeci-Smith model (seven ad hoc closures compared with three in the Cebeci-Smith model) and requires the calculation of a wall distance, y, which restricts the model to wall bounded flows.

8 Beyond the Boussinesq Approximation

As described in section 2.2 the Boussinesq approximation assumes that the Reynolds stress tensor is linearly proportional to the mean stress tensor. This assumption forces the principal axes of these tensors to coincide and the Reynolds stress tensor must therefore be isotropic. However in many flow situations this is not the case. The Reynolds stress tensor is likely to be anisotropic in flows where rapid changes in mean strain rate exist. In the following situations the Boussinesq approximation may fail [67]:

1. Flows with sudden changes in mean strain rate.
2. Flows over curved surfaces.
3. Flows in ducts with secondary motions.
4. Flow in rotating fluids.
5. Three-dimensional flows.
6. Flows with boundary layer separation.

One method for dealing with anisotropic flow is to discard the Boussinesq approximation and use a nonlinear relationship between the Reynolds stress tensor and the mean stress tensor. The most common nonlinear models are Algebraic Stress Models which will be discussed in section 8.2. Second-order closure models go one step further and account for anisotropy by modelling the actual transport equations for each individual component of the Reynolds stress tensor.

8.1 Second-Order Closure Models

In Second-order closure models the Reynolds-stress-tensor is modelled using the Reynolds-stress equations. The Reynolds-stress equations are transport equations for the components of the Reynolds-stress-tensor that are derived by taking the $\overline{u_i' N(u_j) + u_j' N(u_i)}$ moment (where in the Navier-Stokes operator defined in equation (39)) of the Navier-Stokes equations and time- or

ensemble-averaging the product. After considerable algebra we arrive at the Reynolds stress equations,

$$\begin{aligned}\frac{\partial \tau_{ij}}{\partial t} + U_k \frac{\partial \tau_{ij}}{\partial x_k} &= -\tau_{ij}\frac{\partial U_j}{\partial x_k} - \tau_{jk}\frac{\partial U_i}{\partial x_k} + \overline{2\nu \frac{\partial u_i'}{\partial x_k}\frac{\partial u_j'}{\partial x_k}} + \overline{u_i' \frac{\partial p'}{\partial x_j} + u_j' \frac{\partial p'}{\partial x_i}} \\ &\quad + \frac{\partial}{\partial x_k}\left[\frac{\nu}{\rho}\frac{\partial \tau_{ij}}{\partial x_k} + \overline{u_i' u_j' u_k'}\right]. \end{aligned} \tag{93}$$

The Reynolds stress equations are a system of six equations, one for each independent component of the Reynolds-stress-tensor. This system of equations also contains 22 new unknowns. The second-order correlations are now the dependent variables and the new unknowns involve third-order correlations as well as correlations involving gradients of the fluctuating velocities and pressure. The system is not closed which is not surprising since by taking moments of the differential equations we are merely performing mathematical operations, we are not introducing any physical concepts, which would be necessary in order to close this system.

Second-order closure models close the Reynolds-stress equation by replacing the unknowns with coefficients and algebraic expressions that are based upon mean flow properties. The advantage of second-order closure models over eddy-viscosity models is that the Reynolds stress tensor is not treated as an isotropic tensor. However, second-order closure models are computationally very expensive. They require the computation of 6 additional transport equations, and unless strong curvature and secondary recirculation regions are present, little improvement is gained over some of the more advanced eddy-viscosity models. Typically second-order closure models require approximately between 25% to 40% more computing time (depending on the grid and flow situation) than the corresponding two-equation model. Also, the storage of 6 additional variables and their derivatives would take up a considerable amount of computer memory. Reviews of second order closure models are provided by Wilcox [67] and Speziale [54].

8.2 Algebraic Stress Models (ASM)

Algebraic Stress Models (ASM) still use the eddy-viscosity to model the Reynolds stresses, but in ASM the relationship between the Reynolds stresses and the mean flow stresses is not limited to being isotropic. Algebraic Stress Models discard the Boussinesq approximation, and instead use a higher-order, nonlinear representation of the Reynolds-stress-tensor.

ASM are derived from the Reynolds stress equations under the assumption of homogeneous equilibrium turbulence. This equilibrium assumption effectively means that convective and transport effects of the Reynolds stress tensor can be ignored. The most commonly used ASM is the explicit ASM of Gatski and Speziale [19]. This model has been slightly modified since its introduction [55]. These modifications are designed to remove possible singularities that have been shown to arise in solutions were the flow is in strong non-equilibrium. The explicit algebraic stress equation of Speziale et al. [55] is

$$\begin{aligned}\tau_{ij} &= \frac{2}{3}k\delta_{ij} + 2\nu_T\left(S_{ij} - \frac{1}{3}S_{kk}\delta_{ij}\right) - \frac{2\nu_T'\alpha_3}{\omega}\left(S_{ij}\Omega_{kj} + S_{kj}\Omega_{ki}\right) \\ &\quad + \frac{4\nu_T'\alpha_2}{\omega}\left(S_{ik}S_{kj} + \frac{1}{3}S_{kl}S_{kl}\delta_{ij}\right). \end{aligned} \tag{94}$$

The eddy viscosity ν_T is computed using

$$\nu_T = C_\mu \frac{k}{\omega}, \qquad \omega = \frac{\epsilon}{k}, \tag{95}$$

and k and either ω or ϵ are computed using a two-equation model. The closure coefficient in equation (95) is computed using

$$C_\mu = \frac{3(1+\eta^2) + 0.2(\eta^6 + \zeta^6)}{3 + \eta^2 + 6\eta^2\zeta^2 + 6\zeta^2 + \eta^2 + \zeta^2}\alpha_1, \tag{96}$$

where

$$\begin{aligned} \eta^2 &= (\alpha_2/\omega)(S_{ij}S_{ij})^{\frac{1}{2}}, \quad \zeta^2 = (\alpha_3/\omega^2)(\Omega_{ij}\Omega_{ij})^{\frac{1}{2}}, \\ \alpha_1 &= (4/3 - C_2)(g/2), \quad \alpha_2 = (2 - C_3)(g/4), \\ \alpha_3 &= (2 - C_4)(g/4), \quad g = 1/(C_1/2 + C_5 - 1). \end{aligned} \tag{97}$$

The constants are given by

$$C_1 = 6.8, \quad C_2 = 0.36, \quad C_3 = 1.25, \quad C_4 = 0.4, \quad C_5 = 1.88. \tag{98}$$

These constants are calibrated from comparison with a range of strained two-dimensional homogenous turbulent flows near equilibrium. The modified eddy-viscosity, ν'_T is given by

$$\nu'_T = C'_\mu \frac{k}{\omega}, \tag{99}$$

where

$$C'_\mu = \frac{3(1+\eta^2)}{3 + \eta^2 + 6\eta^2\zeta^2 + 6\zeta^2 + \eta^2 + \zeta^2}\alpha_1. \tag{100}$$

ASM models still compute k and ϵ or ω using a two-equation model and hence are limited by this underlying model. Therefore ASM will only provide improvement over standard two-equation models if the Reynolds stress tensor is anisotropic such as in flows with large streamline curvature. Even in anisotropic cases ASM models are unlikely to perform as well as a full second-order closure model. The performances of ASM models will be discussed further in sections 10.2 and 10.4.

9 Surface Boundary Conditions

In order to integrate a turbulence model to a solid surface, boundary values are required at the surface for the velocities and the turbulent parameters for which transport equations are solved. At a no-slip surface the velocities and the turbulent kinetic energy vanish, but the second turbulence parameter is often singular or unknown. For example the specific dissipation rate, ω, varies in the sublayer as y^{-2} (where y is the distance to the surface) approaching the surface. Thus ω is singular at the surface.

9.1 Surface Boundary Conditions for ϵ

Approaching a surface k is proportional to y^2. Since $\epsilon = \omega k$, ϵ has the asymptotic behaviour of

$$\epsilon \propto y^0, \quad \text{as} \quad y \to 0. \tag{101}$$

Therefore the asymptotic behaviour of ϵ does not depend on y. From a perturbation analysis of the boundary layer it can be seen that the asymptotic behaviour of ϵ in fact depends on the near-wall velocities, and unfortunately these are not known a priori [67]. Therefore ϵ can not be specified at a solid surface. The strongest relation for ϵ that we have is

$$\frac{\epsilon}{k} \to \frac{2\nu}{y^2} \quad \text{as} \quad y \to 0, \tag{102}$$

which follows from the viscous sublayer solution for ω.

As previously mentioned, low Reynolds-number (LRN) $k - \epsilon$ models integrate through the viscous sublayer and therefore need a surface boundary condition for ϵ. The general technique for these models is to solve a transport equation in terms of a modified dissipation, $\widetilde{\epsilon}$ instead of solving directly for ϵ. $\widetilde{\epsilon}$ is defined as

$$\widetilde{\epsilon} = \epsilon - \epsilon_0 \tag{103}$$

Model	ϵ_0
Jones-Launder	$2\nu\left(\frac{\partial\sqrt{k}}{\partial n}\right)^2$
Launder-Sharma	$2\nu\left(\frac{\partial\sqrt{k}}{\partial n}\right)^2$
Chien	$2\nu\frac{k}{y^2}$

Table 4: Surface boundary conditions for ϵ_0.

where ϵ_0 is the estimated value of ϵ at $y = 0$, and is defined differently for each LRN model. By using this substitution the convenient dirichlet boundary condition, $\widetilde{\epsilon} = 0$ can be used at the surface, however the estimated value ϵ_0 still needs to be prescribed. The ϵ_0 values used in some common LRN $k-\epsilon$ models are listed in table 4. These boundary conditions all ensure that $k \simeq y^2$ and $\epsilon \simeq 2\nu/y^2$ as $y \to 0$. However there is no other physical reason for their choices. Since the boundary condition for the Chien model does not involve derivatives of k, it is easier to implement and likely to be less numerically stiff.

Lam and Bremhorst (1981) choose to deal directly with ϵ at the boundary by rearranging equation (102) to give

$$k \to \frac{\epsilon y^2}{2\nu} \quad \text{as} \quad y \to 0, \tag{104}$$

which can be differentiated twice to give the ϵ boundary condition,

$$\epsilon = \nu\frac{\partial^2 k}{\partial y^2} \quad \text{at} \quad y = 0. \tag{105}$$

Unfortunately due to the second order derivative, this boundary condition is difficult to implement and leads to problems with numerical stiffness. As an alternative it is common to set the normal derivative of ϵ to zero at solid boundaries. However this is not guaranteed to be physically correct in all flow situations.

9.2 Wall Functions

A common approach when using the $k-\epsilon$ model for wall bounded flows is to forget about the wall boundary conditions altogether and merely set boundary conditions at the first grid point out from the wall. Using the log-law of the wall we can determine the values for the velocities and k and ϵ inside the log-layer region of the boundary layer. Wall functions are algebraic functions that describe the flow properties in the log-region for self-similar boundary layers (the log-law of the wall). As shown in section 1.2, the log law of the wall for the tangential velocity is as follows,

$$U^+ \simeq \frac{1}{\kappa}\ln y^+ + B, \tag{106}$$

By using wall functions we avoid expensive computations in the near-wall region and we can reduce the grid density for wall bounded flows. However it has been shown that the log-law of the wall does not hold for flows with strong pressure gradients or separation [49, 37, 67]. In such situations the wall function approach must be abandoned in favour of a model that can be integrated right down to the wall. It is also important to note that when using wall functions the grid must be designed so that the first grid point out from the wall resides in the log-layer. Grid independent solutions are often impossible with wall-functions since the solutions are sensitive to the placement of this first grid point.

9.3 Zonal Models

Zonal models [7] have also been popular. These models use a one-equation model that solves for k in the near-wall region, thus avoiding modelling ϵ near walls. Since zonal models model

the near-wall region using a differential equation they should provide better results that wall functions for a range of flows, however they do require high grid resolution. For adverse pressure gradients and separated flows using a one-equation model in the near-wall region should be more suitable than merely applying the log-law, however for complicated flows it is likely that a simple one-equation model would still be unsuitable. In these situations, at the minimum we need to solve our two-equation model throughout the boundary layer.

9.4 Surface Boundary Conditions for ω

Unlike ϵ , the asymptotic solution for ω approaching a solid surface is known. The exact solution for ω in the viscous sublayer as derived from a perturbation analysis of the boundary layer [67] is

$$\omega \simeq \frac{6\nu}{\beta_o y^2}, \qquad y^+ < 2.5. \tag{107}$$

If we simply use the value of ω suggested by this solution at the first grid point then there will be significant error in the sublayer solution [67]. It has proven effective to use equation (107) for the first 7 to 10 grid points from the surface provided these points are below $y^+ = 2.5$. This is a common approach when using the $k - \omega$ model.

Saffman discovered that for rough surfaces solutions to the ω-equation exist where ω is finite at the surface [47]. Consequently he proposed that the surface boundary condition for ω be written as

$$\omega = \frac{u_\tau}{\nu} S_R \quad \text{at} \quad y = 0, \tag{108}$$

where u_τ is the friction velocity and S_R is a roughness constant. Sublayer solutions can be computed for arbitrary S_R. The case where $S_R = \infty$ corresponds to a perfectly smooth wall, whereas in the limit $S_R \to 0$ the solutions correspond to very rough surfaces. From these sublayer solutions it is evident that changing the wall value of ω effectively alters the computed constant, B, in the log-law of the wall (equation (106)). In the limit $S_R \to 0$, the numerical results indicate that

$$B \to 8.4 + \frac{1}{\kappa} \ln\left(S_R/100\right) \quad \text{as} \quad S_R \to 0. \tag{109}$$

As reported in [48], Nikuradse performed experiments on rough surface flows and found that

$$B \to 8.5 + \frac{1}{\kappa} \ln(1/k_s^+), \qquad k_s^+ = u_\tau k_s/\nu, \tag{110}$$

where k_s is height of the sand-grain roughness elements. These two equations are nearly identical if

$$S_R = 100/k_s^+, \qquad k_s^+ >> 1. \tag{111}$$

Using this form for the ω surface boundary condition yields excellent results for flows involving rough walls.

Wilcox and Chambers [64] used an argument based on the flow over a wavy wall to show that for small roughness heights it is suitable to use

$$S_R \propto (1/k_s^+)^2 \quad \text{as} \quad k_s^+ \to 0. \tag{112}$$

Combining this relation with our ω surface boundary condition (equation (108)) yields the slightly-rough-surface boundary condition for ω, viz.,

$$\omega = \frac{2500\nu}{k_s^2} \quad \text{at} \quad y = 0. \tag{113}$$

Following equation (112), k_s must be set small enough to ensure $k_s^+ < 5$ which corresponds to a hydraulically smooth surface. If a k_s value is used that is too large then the computed skin-friction values will be overpredicted.

As an example of the application of this method consider a surface that is approximated with a sandgrain roughness of $k_s = 0.0001$m (or 0.1mm), which is of the same order of magnitude that can be expected for sailcloth. For this example the appropriate boundary condition for ω at the surface would be

$$\omega = 447.25 \quad \text{at} \quad y = 0. \tag{114}$$

Using larger ω values would correspond to smoother surfaces. Ideally computations should be repeated using a range of ω values at the boundary to determine the sensitivity of the solution on this value and the surface roughness that best suits experimental data for the particular surface. It is envisioned that large surface values of ω will be necessary to maintain the accuracy of the asymptotic solution for ω. Therefore numerical issues are likely to arise in defining the derivative of ω across the cells adjacent to the wall since this derivative is likely to also be large.

Menter uses an alternative formulation of the ω surface boundary condition for hydraulically smooth walls [33]. Menter attempts to match the asymptotic behaviour of ω using a discrete representation of ω across the viscous sublayer. In his approach the ω value at the surface is dependent on the distance to the first grid point out from the surface, Δy_2, i.e.,

$$\omega = \frac{N\nu}{(\Delta y_2)^2} \quad \text{at} \quad y = 0, \tag{115}$$

where N is a constant. In comparison to the method of Wilcox and Chambers, this corresponds to setting roughness heights according to

$$\frac{2500\nu}{k_s^2} = \frac{N\nu}{(\Delta y_2)^2} \Longrightarrow k_s^+ = \frac{50\Delta y_2^+}{\sqrt{N}}. \tag{116}$$

If N is chosen to be 100 then for all $\Delta y_2^+ < 1$, the surface roughness, k_s^+, will be less than 5. Therefore hydraulic smoothness is guaranteed. The drawback of Menter's approach is that the boundary condition is grid dependent. However experimentally it has been shown that deviations in k_s^+ have minor influence on solutions, so long as k_s^+ remains below 5.

Patel, Chon and Yoon investigate turbulence modelling of flows over rough surfaces including a flow that involves separation [37]. They compare both the standard $k-\omega$ model and the two-layer based $k-\epsilon$ model of Chen and Patel [7] with experimental results. The $k-\epsilon$ model uses a one-equation model in the viscous sublayer that is designed to take into account the effects of surface roughness. Results show that the $k-\omega$ model performs well over a wide range of roughness values, while the $k-\epsilon$ model gave much poorer results. The results indicate that the $k-\omega$ model can be used for k_s^+ up to 10^4, which is much higher than the value of 400 that Wilcox suggests [67]. Comparatively the $k-\epsilon$ model was inaccurate for all roughness values. For the separated flow case the results indicate that the $k-\omega$ model can handle separation in rough-surface flows well. However it must be noted that the sandgrain sizes that are used correspond to values of up to 70, and so the surface is not hydraulically smooth. Therefore these results provide little evidence that the surface roughness boundary condition for ω is suitable for flows over hydraulically smooth surfaces such as sails.

10 Turbulence Modelling for Sail Flows

10.1 The Nature of Sail Flows

In order to understand the requirements of a turbulence model that is to be used for modelling downwind sail flows it is important to understand the specific flow situation. Consider figure 4, a bird's-eye perspective of a yacht travelling downwind. The aerodynamic forces on the yacht are

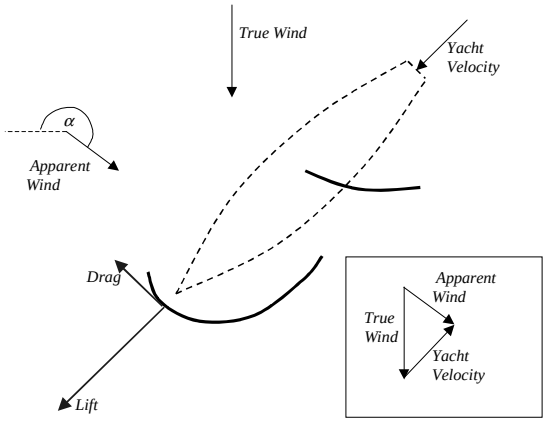

Figure 4: Aerodynamic forces on a yacht sailing downwind.

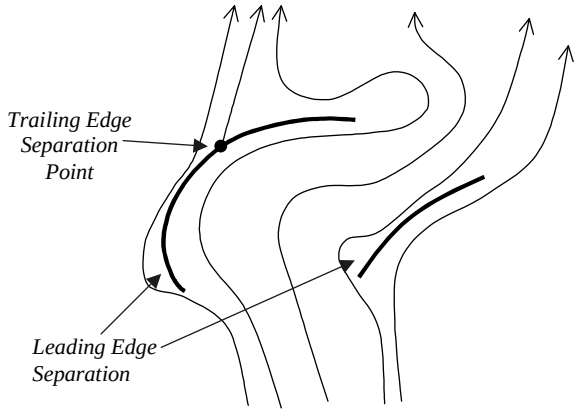

Figure 5: A downwind sail flow.

resolved into lift and drag forces. By definition the lift force points in a direction perpendicular to the apparent wind, while the drag points in the same direction as the wind (the apparent wind is the wind vector relative to the velocity of the yacht). As is illustrated in figure 4, it is common when sailing downwind for the apparent wind to come directly from the windward side of the yacht. If the apparent wind is in fact perpendicular to the yacht's fore-aft axis then the lift force points in the same direction as the boat is travelling. Therefore all of the lift force goes into driving the boat and the drag force has little effect on boat speed (drag is balanced by the hydrodynamic force of the keel). The downwind sail configuration can be classed as a high-lift system; it can be optimised to give maximum lift while giving little consideration to the drag force. The flow field around a downwind sail configuration is illustrated in figure 5.

Noticeable features of the flow in figure 5 that present difficulties for turbulence models are:

1. The leading edge separation bubbles on both sails. The flow accelerates around the leading edge and subsequently separates, forming a recirculation region. The boundary layer then reattaches further down the sail. When a sail stalls (as it does when travelling directly downwind) the leading edge separation region never reattaches and instead forms a disrupted flow region downstream of the sail.

2. The trailing edge separation on the suction surface of the genneker. This is caused by an

adverse pressure gradient that retards the flow.

3. The genneker itself, and the flow streamlines are highly curved. Curvature introduces anisotropy in the Reynolds stress tensor.

4. The flow over each sail is dependent on the flow over the other.

The flow situation for yacht sailing upwind is a much simpler problem to model. Upwind sails operate like most aerofoils, their design is aimed towards maximising the lift to drag ratio. Therefore particular importance is paid to minimising drag at the same time as maximising lift. Generally the flow remains attached and there is much less streamline curvature than for downwind flows. Therefore it is conceived that a model that is suitable for evaluating downwind sail flows will by default be suitable for upwind flows as well. However it may be desirable to use a simpler model for upwind flows that requires lower computational resources. Such a model would still require some degree of sophistication. It was shown in [12] that due to adverse pressure gradients, the wall function treatment of the inner layer is still unsuitable for upwind flows. The Spalart-Allmaras model [52] has gained success for aerodynamic applications and is likely to also perform well for upwind sail flows. This model is less demanding than two-equation models and can be integrated throughout the viscous sub-layer.

The mast which supports the mainsail has considerable influence on the flow. Design of mast sections is a crucial element of yacht aerodynamics and therefore consideration of the mast must be applied when implementing a turbulence model for sail flows. The flow past a mainsail with a mast is shown in figure 6. A small separation bubble can be seen on the suction surface at the trailing edge of the mast. It is important that the model provides an accurate prediction of this separation point as it has significant influence on the overall lift and drag of the mast-sail combination.

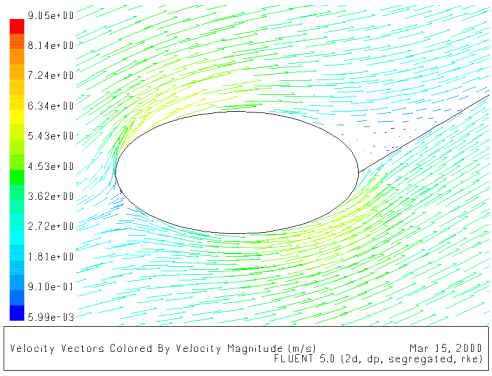

Figure 6: Flow past a mast section.

Downwind sail's operate like high-lift aerofoils, the lift force is maximised while little regard is paid to the drag force. Modelling high-lift foils is particularly difficult due to the high angles of attack that they operate at. These foils are used in landing and take off of aeroplanes and consequently a lot of attention has been paid to modelling high-lift flows. Section 10.2 will be dedicated to turbulence modelling for high-lift flows. Adverse pressure gradients and separation will be discussed in section 10.3. Historically turbulence models have given poor results in these regions. Section 10.4 will be discuss the effects of streamline curvature, which is particularly important for modelling downwind sails. One of the main goals of upwind sail design is reducing the vortices that develop at the head and foot. Therefore it is important that a turbulence model resolve these accurately. Modelling vortices is discussed further in section 10.5. Turbulent transition will be discussed in section 10.6, and some common approaches to transition modelling will be presented. The treatment of the inlet turbulence conditions will be discussed in section 10.7. The onset flow to a sail is always unsteady to a degree, and the position of the separation point

(if separation is present) may oscillate. Therefore we need a turbulence model that accurately predicts transient behaviour. Unsteady flow will be discussed in section 10.8.

10.2 Modelling High-Lift Foils

The aerospace and aircraft industries invest extensive resources into aerofoil design and analysis. Consequently there has also been comprehensive research in the field of high-lift aerofoils. Traditionally algebraic turbulence models have been the models of choice for aerodynamic applications. This is due to their simplicity and efficiency. Algebraic models can be easily altered to suit particular applications, and solutions converge significantly faster than models that solve transport equations. However for flows where length scales vary widely through the flow domain, these models are likely to be inaccurate. High-lift foils often involve separation regions where an algebraic specification of the length scale is inappropriate. Moreover, algebraic models are inappropriate for use with multi-element high-lift systems (such as a configuration of two sails) due to the interaction the wake of the first foil has with the flow over the second foil. Consequently over the last decade one- and two-equation turbulence models have gained popularity for high-lift flows.

For high-lift flows the Spalart-Allmaras model and Menter's SST model have frequently stood out among one- and two-equation turbulence models. These two models seem to model adverse pressure gradients and separation better than most other models. This makes good sense since they have been calibrated for these types of flows. Godin, Zingg and Nelson compared these two models using several high-lift flows [20]. They discovered that for attached flows both models gave excellent results, however for separated flows the SST model was able to model the recirculation region with higher accuracy. The SST model is a two-equation model and can therefore be expected to suitably model a wider range of flow situations (see section 6.5) than the one-equation SA model. They conclude that the Spalart-Allmaras model is more robust, especially for attached flow over multi-element foils. This is due to the transport equation for the eddy-viscosity which has the convenient wall boundary condition, $\nu_T = 0$, and hence does not involve the surface boundary condition problems of ϵ and ω at boundaries (see section 9). Therefore the Spalart-Allmaras model could be more suitable for upwind sail flows where the flow generally remains attached.

S. Kim, C. Kim, and Rho compute flows over single and multi-element foils using the standard $k-\epsilon$, standard $k-\omega$ and SST models [24]. Flows are computed over a range of angles of attack. The SST model consistently outperforms the other models and in particular the model gives much better velocity profiles, especially in separation regions. At high angles of attack the $k-\omega$ model outperforms the $k-\epsilon$ model. This is not surprising since Wilcox has shown that his model resolves adverse pressure gradients better than the $k-\epsilon$ model [67]. The performance of the $k-\omega$ and $k-\epsilon$ models for adverse pressure gradients is discussed in greater depth in section 10.3.

Yang, Chang and Arici compute the flow over a high-lift aerofoil using a variant of the $k-\omega$ model [69]. To remove dependence on freestream values they introduce cross diffusion to the ω-equation. Instead of using a blending function, they introduce cross diffusion when it is positive (which generally occurs outside of the viscous sublayer), and without damping. Therefore the model should behave much like a Low Reynolds Number (LRN) $k-\epsilon$ model. The results are good for flows at low angles of attack, but deteriorate as this angle is increased above 10 degrees, where flow separation begins to occur. They note that by altering ("twiggling") the coefficient for the production terms in the k- and ω-equations, better accuracy can be gained for separated flows. They conclude that a new formulation for these production terms needs to be developed for separated flows.

Due to large streamline curvature, flow separation and recirculation, high-lift flows are likely to exhibit anisotropy of the Reynolds stress tensor. Recently several Algebraic Stress Models (ASM) have been used for high-lift flows, with moderate success. Abid, Rumsey and Gatski [2] compute several high-lift flows using the explicit algebraic stress equation derived by Gakski and Speziale [19]. The algebraic stress equation is used in conjunction with both the standard $k-\epsilon$ and standard $k-\omega$ models. The two models are compared with the standard $k-\omega$ model

and a two-equation $k-\epsilon$ model of Abid [1] (known as the AB model), which is designed for transitional flows. One of their test cases is the highly cambered NACA4412 aerofoil at maximum lift ($\alpha = 13.87°$) which was tested experimentally by Coles and Wadcock [9]. This test case is popular for modelling high-lift conditions and has been used by many authors in validating and comparing turbulence models. The Reynolds number of the flow is 1.52×10^6 (based on chord length), which is a Reynolds number typical of sail flows, albeit at the lower end of the scale. For this flow the $k-\omega$ based ASM model gives excellent results, the standard $k-\omega$ model predicts too little separation, the $k-\epsilon$ based ASM model predicts slightly too much separation, and the AB model gives satisfactory results. However for the other test cases the AB model does not perform as well as the $k-\omega$ models. The ASM models provide improvement over the standard two-equation models for anisotropic flows because of their ability to account for non-equilibrium effects. However in this study the choice of the form of the two-equation model (i.e. $k-\epsilon$ or $k-\omega$) has a more dramatic influence on the results, with the $k-\omega$ based ASM outperforming the $k-\epsilon$ ASM. It is important to note that there is always an uncertainty over published results for the standard $k-\omega$ as the model's dependency on freestream values can create unrealistic errors if these values are not chosen correctly.

Rumsey, Gatski, Ying and Bertelrud [46] compare the Spalart-Allmaras model, the SST model and the explicit ASM of Gatski and Speziale [55] (in a $k-\omega$ formulation) on two multi-element high-lift aerofoil systems. Although some variations between the models are evident, the non-linear ASM predicts similar lift and drag coefficients to the linear models [46]. In the test cases there is no boundary layer separation and Reynolds stress tensor can be expected to be essentially isotropic. For flows at much higher angles of attack with high curvature and large separation regions the anisotropy of the Reynolds stress tensor is more likely. Such a situation occurs in downwind sailing, and here ASM may produce better results than the SST and SA models.

High-lift flows such as the flows described in this section are very demanding and challenge the assumptions from where two-equation models are derived. Downwind sail flows are even more challenging. While both types of flow operate at similar high angles of attack, downwind sails generally have much larger camber and consequently exhibit large streamline curvature and big separation regions. Consequently the flow around downwind sails is more likely to be in non-equilibrium and to be anisotropic. Therefore a minimum requirement for a turbulence model that is to be used for downwind sails is that it should be accurate for high-lift flows. However even models that perform well for these flows may struggle to resolve the complicated turbulent flow field around downwind sails.

10.3 Adverse Pressure Gradients and Separation

On the leeward (or suction) side of an aerofoil (or sail) an adverse pressure gradient forms that retards the flow in the boundary layer. As the angle of attack is increased this pressure gradient increases in strength until the leeward boundary layer becomes stalled at some length down the aerofoil (the separation point) and the flow detaches from the surface forming a separation bubble. In figure 7a the adverse pressure gradient is not strong enough to cause separation. In figure 7b the pressure gradient on the leeward side of the foil is stronger due to a higher angle of attack. Consequently the flow separates.

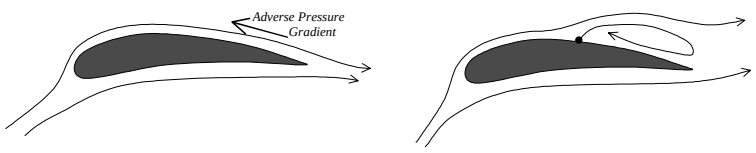

a. Attached flow. b. Separated flow.

Figure 7: Flow separation due to an adverse pressure gradient.

Wilcox [67] computes 16 different boundary layer flows in varying adverse pressure gradients

using the standard $k-\epsilon$ model and the $k-\omega$ (1998) model. For the majority of the flows the $k-\omega$ model predicts excellent skin-friction distributions. As the adverse pressure gradient increases in strength the $k-\epsilon$ model gives progressively poorer estimations of the skin friction. Only for one flow (which was the only separating flow), does the $k-\omega$ model give significantly inaccurate results. For this flow the $k-\omega$ model overpredicts the skin friction coefficient by a maximum of 55%, while the $k-\epsilon$ model predicts skin friction values 4 times as large as the experimental data.

Wilcox [67] also compares the $k-\epsilon$ and $k-\omega$ models in a perturbation analysis of the defect layer. For flow with no pressure gradient both models predict velocity profiles that fall within 3% of the experimental data. When a strong adverse pressure gradient is introduced the $k-\omega$ model still produces results within 3%, whereas the $k-\epsilon$ model is in error by up to 25%. Wilcox shows that in an adverse pressure gradient the $k-\omega$ model predicts a smaller turbulent length scale in the defect layer, therefore the eddy-viscosity is also lower. Hence the $k-\omega$ model predicts a less diffusive flow and consequently lower skin-friction (since there will be less turbulent shear stress) and separation is likely to occur earlier. The superior performance of the $k-\omega$ model for adverse pressure gradients can be largely attributed to its performance in the defect layer. The largest discrepancy between the $k-\epsilon$ model and the experimental data occurs at the inner edge of the defect layer. Towards the outer edge of the layer the $k-\epsilon$ model predicts velocities close to the experimental data for both zero pressure-gradient and adverse pressure-gradient flows. Recall that Menter's BSL and SST models blended from $k-\omega$ to $k-\epsilon$ across this layer. Therefore Menter's models should perform well for adverse pressure gradients, despite behaving like the $k-\epsilon$ model towards the outer edge of the defect layer.

Menter [30] compares the performances of the following turbulence models for several attached and separated adverse pressure gradient flows:

1. Baldwin-Lomax (BL) (algebraic (zero-equation) model, 1978) [4]
2. Johnson-King (JK) (half-equation model, 1985, 1990) [22, 21]
3. Baldwin-Barth (BB) (one-equation model, 1990) [3]
4. Wilcox Model ($k-\omega$) (two-equation model, 1988) [60].

The three transport equation models gave consistently better results than the algebraic model of Baldwin and Lomax. Overall the JK model gave the best agreement with the experimental data. However the model does have a tendency to give somewhat high maximum shear-stress levels in adverse pressure gradients, albeit lower than the other models. The $k-\omega$ model consistently over-predicted the Reynolds shear-stress levels. On eof the test cases was Driver's separated flow, which involves an adverse pressure gradient developing in the axial direction in the axisymmetric flow along a circular cyliner [15]. In the separation region the experimental data shows a flattening of the pressure coefficient. All models underpredict this effect. In this region the JK model overpredicts the pressure coefficient by a maximum of 6.7%, the BB model by 9.3%, the $k-\omega$ model by 11.1% and the BL model by 20%. Menter blames the poor performance in the separation region on the over-prediction of turbulent shear stress near the separation point.

The performance of the Johnson-King model is surprising considering the model's simplicity. The JK model solves a single ordinary-differential-equation (ODE) for the streamwise development of the maximum Reynolds shear stress. The profile for the turbulent shear stress across the boundary layer is computed using an algebraic specification as with any algebraic model. However when the flow departs from turbulent equilibrium the ODE adjusts the magnitude of the shear stress profile.

After noting the success of the JK model, Menter recomputed the separated flow case for the $k-\omega$ model using a modified eddy-viscosity relation based upon Bradshaw's assumption. His modified eddy-viscosity relation for adverse pressure gradient flows is given by

$$\nu_T = \frac{a_1 k}{S}. \tag{117}$$

The modified $k-\omega$ model produced better results for the separation region with pressure being overpredicted by a maximum of 4.8%. Moreover the maximum shear-stress levels were lower and much closer to the experimental data than those computed using the original model. This experience lead to the development of the SST relation (equation (58)) which blends from equation (117) in adverse pressure gradient flows to the standard eddy viscosity relation (equation (45)) elsewhere.

10.4 Curvature

Upwind sails are only curved slightly and curvature effects can be expected to be negligible. Conversely, downwind sails are generally highly curved. The curvature involved in downwind sail

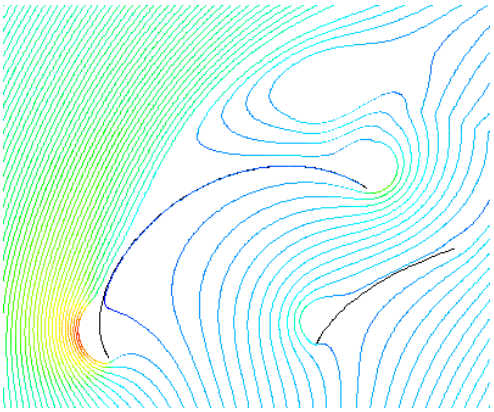

Figure 8: Two-dimensional flow past a downwind sail. Computed using FLUENT 5.0.

flows is likely to introduce anisotropy in the Reynolds stress tensor. Therefore it is necessary to assess (using a suitable validation study) any inaccuracies that may arise for turbulence models used to model such flows.

The effects of streamline curvature in a laminar flow are of $\mathcal{O}(K\delta)$, where K is the surface curvature. Experimental evidence suggests that for turbulent flows curvature effects are an order of magnitude larger [**?**] than order $\mathcal{O}(K\delta)$. The second order terms truncated in the Boussinesq approximation are of order $\mathcal{O}(K\delta)$, therefore there is a direct influence of curvature on the Reynolds stresses beyond their relationship with the mean rate-of-strain tensor. That is, curvature directly impacts upon the terms that describe physical processes involving interactions between turbulent fluctuations such as turbulent diffusion, pressure redistribution and destruction by viscous action [**?**].

Experiments have shown that the physical processes involved with convex and concave boundary layers are quite different [**?**]. In a convex boundary layer curvature acts to suppress the Reynolds stresses and thus separation is enhanced. For concave curvature the effect is the opposite with the Reynolds shear stress being enhanced with possible relaminarization. Analogy is often made between flows subject to streamline curvature and flows subject to pressure gradients. Convex boundary layers behave like adverse pressure gradient flows and concave boundary layers behave like flows subject to favourable pressure gradients. Not unlike flows subject to large pressure gradients, the log-law of the wall does not hold for strong curvature. For convex curvature velocity profiles lie above the log-law and for concave curvature they lie below the log-law. Consequently wall functions should only be used with great caution for flows exhibiting considerable streamline curvature.

For convex curvature the response to strong curvature can be considerable. The ratio of the Reynolds shear stress, τ to k (i.e. a_1) can decrease to considerably lower than 0.3 and thus Bradshaw's relation for the Reynolds shear stress is unsuitable.

Streamwise variations of mean velocities have been observed in concave turbulent boundary layers and several authors have suggested that Taylor-Görtler vortices may be present [**?**]. Shear stresses in the transverse (third dimension), $\overline{u_\theta w}$ and $\overline{u_r w}$, have been observed in concave boundary layers to be of the order of $0.25\overline{u_\theta u_r}$, and their signs reversed over distances of order 0.5δ [**?**]. However there is conflicting evidence regarding the existence of stable Taylor-Görtler vortices. For example Jeans and Johnson observed that these three-dimensional structures did not have well defined cores of concentrated vorticity [**?**]. They concluded that the structures could not be regarded as vortices and instead suggested the term "roll cells". However there is no discrepancy in the fact that the physical mechanisms underlying concave boundary layers are unique and turbulence models that perform well for convex boundary layers may be unsuitable for concave boundary layers.

For a two-dimensional incompressible boundary layer on surface with curvature K, the modelled k-equation can be written in polar coordinates as,

$$U_\theta \frac{\partial k}{\partial \theta} + U_r \frac{\partial k}{\partial r} = \nu_T \left(\frac{\partial U_\theta}{\partial r} - K U_\theta \right)^2 - \epsilon + \frac{\partial}{\partial r} \left[\left(\nu + \sigma^* \nu_T \right) \frac{\partial k}{\partial r} \right], \tag{118}$$

where U_θ and U_r represent the velocity components in directions tangential (θ) and normal (r) to the surface. This boundary layer equation can be rewritten,

$$U_\theta \frac{\partial k}{\partial \theta} + U_r \frac{\partial k}{\partial r} = \nu_T \left(1 - S_*\right)^2 \left(\frac{\partial U_\theta}{\partial r} \right)^2 - \epsilon + \frac{\partial}{\partial r} \left[\left(\nu + \sigma^* \nu_T \right) \frac{\partial k}{\partial r} \right] \tag{119}$$

where S_* is the ratio of the extra rate-of-strain (KU_θ) to the primary rate ($\partial U_\theta / \partial r$),

$$S_* = \frac{K U_\theta}{\partial U_\theta / \partial r} \tag{120}$$

In equation (119) curvature is present only in the production term through the extra strain-rate parameter, S_*. For convex curvature, $S_* > 0$, acts to reduce k and thus also the Reynolds shear stresses as observed in experiments. Concave curvature, $S_* < 0$, has the opposite effect. However these effects will be proportional to S_*^2 and not an order of magnitude larger as suggested by experiment. Therefore the k-equation does not fully account for curvature effects and modifications are necessary.

It is possible to gain improvement in accuracy for flows over curved surfaces by incorporating ad hoc curvature corrections. From analogy with the transport of normal Reynolds stresses, Wilcox and Chambers proposed a curvature correction to the k-equation [65]. They introduced the following term to the left-hand side of equation 118,

$$\frac{9}{2} \nu_T K U \frac{\partial U_\theta}{\partial r}. \tag{121}$$

This term is designed to account for the transport of normal Reynolds stresses which have been ignored in the original model. This term reduces the production of k in regions of convex curvature and enhances the production of k in regions of concave curvature. The coefficient, $9/2$, has been calibrated from comparison to experimentals around curved surfaces. Similar modifications have been made to the ϵ-equation through alteration of the generation and destruction terms (for example Launder et al [**?**]). Models have also be formulated using a variable C_μ coefficient in the eddy-viscosity relation. These models are designed so that the eddy-viscosity is reduced in regions of convex curvature and increased in regions of concave curvature (for example, Gibson [**?**]).

Ad hoc corrections have in the past produced acceptable predictions of mean flow quantities such as skin friction, surface pressures and mean velocities for flows with large streamline curvature (see Wilcox [67]). However this is only through extensive calibration and such models are likely to be unreliable. Ad hoc curvature corrections cannot adequately reproduce the

Reynolds stress tensor as this tensor is anisotropic for highly curved flows. Therefore a higher-order representation of the Reynolds stresses is preferred for flows with considerable streamline curvature.

Algebraic stress models provide some level of improvement for curved flows. Luo and Lakshminarayana investigated the two-dimensional flow in U-shaped duct using several models of varying complexity [**?**]. They compared the Reynolds stress model (RSM) of Gibson and Launder [**?**] with an ASM, a second-order non-linear eddy-viscosity model (non-ASM) and the standard $k-\epsilon$ model. The ASM provided considerably improved profiles of both k (using $k = 0.5(\overline{uu}+\overline{vv})$) and the Reynold shear stress in both convex and concave regions of the flow when compared with the solutions computed by the standard $k-\epsilon$ model. A similar study of this flow by Rumsey, Gatski and Morrison has shown that in the convex boundary layer (inner wall) the ASM provides no significant improvement over the SST model in the Reynolds shear stress profiles. However for the concave wall the ASM performs significantly better than the SST model [45].

In their study of the two-dimensional U-shaped duct Rumsey at al investigate the behaviour of the anisotropy tensor,

$$b_{ij} = \tau_{ij}/2k - \frac{1}{3}\delta_{ij}, \tag{122}$$

using the RSM. They discover that Db/Dt is significantly non-zero near the convex wall and thus the assumption of homogeneous equilibrium ($Db/Dt = 0$) that is used in the derivation of the ASM is invalid. Subsequently they relax the equilibrium condition by imposing it in a locally varying noninertial coordinate frame throughout the flow. That is, the principle axis of the anisotropy tensor is rotated to align with the local coordinate frame and the equilibrium condition is applied to this new tensor rather that explicitly to b.

The transformation of the anisotropy tensor, b^q_p, to the local principle axis coordinate frame is given by,

$$\overline{b}^j_i = \underline{X}^p_i b^q_p \overline{X}^j_q \tag{123}$$

where $\overline{X}^j_q$ is the orthogonal tensor that represents the transformation to the local principle axis coordinate frame. The material derivative of this transformed anisotropy tensor is given by,

$$\frac{D\overline{b}^j_i}{Dt} = b^k_p \underline{X}^p_i \frac{Db^q_p}{Dt}\overline{X}^j_q + \frac{D\underline{X}^p_i}{Dt} b^q_p \overline{X}^j_q + \underline{X}^p_i b^q_p \frac{D\overline{X}^j_q}{Dt}. \tag{124}$$

If the equilibrium assumption is now applied in the transformed coordinate frame so that, $\partial \overline{b}^j_i/\partial t = 0$, equation(124) reduces to,

$$\frac{Db^q_p}{Dt} = b^k_q \Omega^p_k - b^k_p \Omega^q_k, \qquad \Omega^q_p = \underline{X}^k_p \frac{D\overline{X}^q_k}{Dt}. \tag{125}$$

When this inhomogeneous equilibrium condition is used in place of the homogeneous equilibrium condition the ASM responds much more admirably to streamline curvature. Somewhat surprisingly the new model gives better results than the RSM for the convex boundary layer of the U-shaped duct. Unfortunately concave boundary layer profiles were not investigated.

10.5 Tip Vortices

Due to pressure equalisation at the head and foot of sails, large vortices develop in the wake. These can be seen in figure 9. These vortices constitute a loss of momentum from the flow, and consequently they induce a force. The induced drag from tip vortices is the major contributor to the total drag on a sail configuration. Consequently reducing the adverse influence of these vortices is one of the primary goals of the sail designer. Therefore in order to produce a suitable design tool it is essential that a turbulence model resolves these vortices adequately.

An investigation of turbulence modelling for vortex flows was carried out by Svennberg [58]. This investigation looked at the following eight turbulence models:

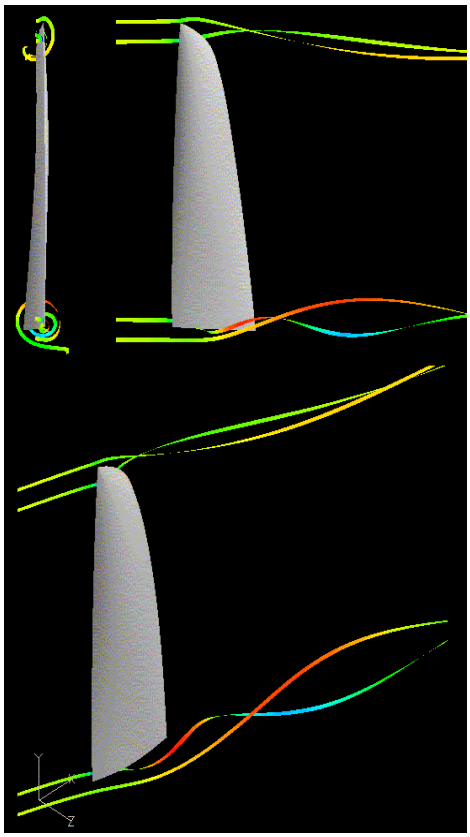

Figure 9: Vortices in the wake of an IACC mainsail.

- The standard $k-\epsilon$ model [23],
- The RNG $k-\epsilon$ model [68],
- The standard $k-\omega$ model [60],
- The BSL model [34, 35],
- The SST model [34, 35],
- The algebraic stress model by Gatski and Speziale (GS) [19],
- The algebraic stress model by Craft, Launder and Suga (CLS) [13, 14], and
- The Reynolds stress transport model (RSM) by Launder and Shima [27].

Three test cases were used in the analysis:

- A vortex in a free-stream,
- A vortex pair embedded in a boundary layer, and
- The flow around the KVLCC2 tanker, where an induced vortex develops around the curved surface of the bilge.

The vortex pair embedded in a boundary layer is of particular importance as it presents a similar situation to the wake from an upwind sail. The only difference is that the vortices are

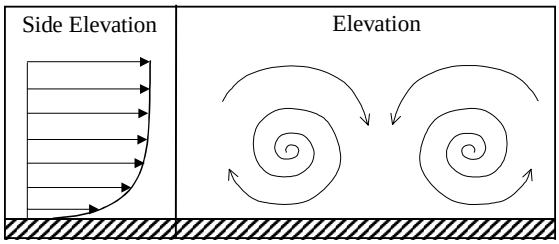

Figure 10: A vortex pair embedded in a boundary layer.

aligned horizontally in the boundary layer, whereas in the wake of a sail they are vertical. The vortices were generated using two half-delta wings mounted on the wind tunnel floor. The flow in the wake of these vortex generators is illustrated in schematic form in figure 10. In order to lessen the computational requirements the computational domain for the simulations is positioned downstream of the vortex generators. Unfortunately the experimental data was at a resolution that was too low to use as inlet data. To overcome this problem the inlet data was generated using the RSM model.

All of the models performed quite poorly for this test case and in general predicted the vortices to dissipate early. Also of concern was that the models positioned the core of the vortex with poor accuracy. For the vertical positioning of the vortex at the end of the test section the $k-\omega$ model gave the worst result and was in error by approximately 21%. The RSM and RNG models gave the most accurate positions but were still in error by approximately 7%.

For this test case the models all underpredict the turbulent kinetic energy at the vortex core and give values that are too high in the remainder of the vortex. Consequently the eddy viscosity is overpredicted and the vortex decays faster than the experimental results indicate. However there are some positive points to note. The RSM model gives results in reasonably good agreement with the data and was certainly the most successful of the models. This illustrates the importance of modelling anisotropy of the Reynolds stress tensor for flows with large streamline curvature. Consequently the ASM models also performed well. The RNG model gave excellent results considering its simplicity. Its results were judged to be as good as the GS model and almost as good as the CLS model. The RNG model includes a term in the ϵ-equation designed to account for streamline curvature. The success of this model illustrates that ad hoc modifications have real promise when suited to the specific application. The SST model performed better than the other models, this is due to the SST eddy viscosity condition that is active near walls. The $k-\omega$ model performed poorly which was surprising. However there is considerable uncertainty in the inlet data that was used. Therefore it is likely that the $k-\omega$ is suffering due to its dependency on freestream values. It would have been interesting to see how the 1998 version performs for this test case.

The flow around the KVLCC2 tanker showed very different trends in the results. It is important to note that grid independence was not obtained and there is considerable uncertainty to the results. Nevertheless for general comparison between the models the results should still be valid.

For this flow the SST model gave the best results. This is due its special treatment of the Reynolds stresses for adverse pressure gradients. The $k-\omega$ model, (which is also known to perform well in adverse pressure gradients) showed a large improvement for this flow. All the other models (except for the BSL model) suffered due to their inadequate near-wall treatments. Each of these models predicted vortices that were initially much weaker than the experimental data. However the RSM, ASM and RNG models managed to sustain the vortex strength further downstream in the wake than the other models.

The study was mainly concerned with the flow profiles in the plane of the propeller (the propeller was not included in the simulations) and here the SST model gave the most accurate results. However further downstream the SST model predicted the vortex to decay earlier than

the experimental results indicated. The RSM model on the other hand, sustained the vortex for a longer distance downstream. This illustrates an important point, the RSM model outperforms all the other models in just about all the important modelling facets: streamline curvature, anisotropy, non-equilibrium and adverse pressure gradients, but it has problems in the near-wall. Conversely the SST model can model adverse pressure gradients and the near-wall well, but cannot handle streamline curvature and anisotropy. Consequently the SST model performs the most suitably in the immediate vicinity of the ship and the RSM model is the model of choice for the wake region. Therefore a model that merges between the two models would have the potential to provide the best of both worlds. Potentially such a model would not require a large increase in computational resources. For flows involving walls the major computational demand is near-walls were fine grid spacing must be employed. In the wake region where the more advanced model is needed the required grid spacing is several orders of magnitude larger. Moreover, since an RSM model is likely to produce more accurate results than a two-equation model, it is likely that grid requirements for the vortex region could be less stringent if the RSM model was used. Therefore using RSM for wake flows could potentially provide solutions more efficiently than a two-equation model, if the same accuracy is desired. However developing such a model would be an extremely arduous task, a much more simple solution would be to use an algebraic stress equation or a curvature correction (such as that used in the RNG model) in the vortex region.

It is necessary to fully evaluate the importance of modelling the wake region before developing such advanced models. A suitable study would investigate the effects of grid density in the wake region. By solving the flow on a coarser grid we are effectively introducing numerical diffusion that would cause the tip vortices to decay earlier. Therefore if a flow where the wake decays early produced significantly different loads on the sail to a solution with high grid density in the wake, then it would be obvious that the accuracy of the solution in the wake region has an important effect on the flow near the sail. From potential flow analysis we know that the induced velocities from a singular vortex are proportional to $1/r$, where r is the distance from the centre of the vortex. Therefore the influence that a vortex in the wake has on the flow near the sail decreases the further it is downstream of the sail.

The vortex-lattice method is used in potential flow codes which are commonly used in sail analysis [18]. The vortex-lattice method models tip vortices using singular vortex lines. That is, lines extending from the head and foot of the sail about which the flow circulates. Moreover at the vortex core the radial velocities are singular. For viscous flows this singularity cannot exist and the radial velocities vanish at the core. The differences between singular vortices and a viscous (real) vortex are illustrated in figure 11.

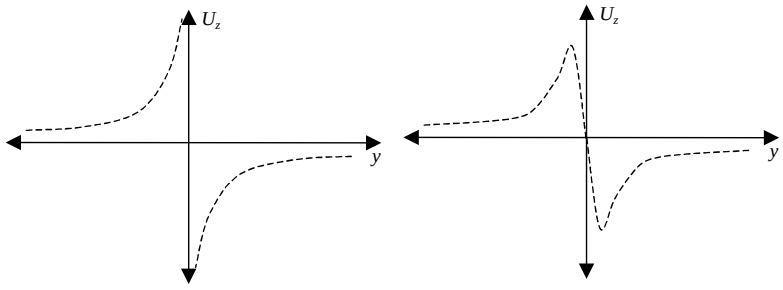

a. A singular vortex b. A vortex in viscous flow

Figure 11: Vortex types. U_z represents vertical velocity and y represents the horizontal direction (both these directions are perpendicular to the axial direction of the vortex).

At the vortex core the radial velocities are overpredicted for the singular vortex. However since this region near the core is small the approximation is still reasonable. In the vortex-lattice method the vortex-lines extend an infinite distance downstream and have a constant vortex strength. Whereas in reality the vortex decays as molecular and turbulent diffusion transports momentum from the vortex out into the mean flow. In the RSM calculations for the vortex pair

test case in [58], the maximum radial velocities had decayed to approximately half their initial values at a distance $13L$ downstream from the start of the computational domain (where L is the separation between the vortex cores). For sail flows the potential flow assumption of constant vortex strength would certainly have an adverse influence on results. However vortex-lattice codes are usually altered so that numerical results are in line with experimental testing.

10.6 Transition Modelling

Standard two-equation turbulence models cannot be used to describe transition from laminar to turbulent flow. In fact, standard turbulence models predict transition at Reynolds numbers that are at least an order of magnitude too low. For the case of the flow past a sail or an aerofoil this corresponds to transition occurring well upstream of the desired location. Positioning of the transition point can potentially have a large influence on lift and drag values. A turbulent boundary layer exhibits considerably more skin-friction than a laminar boundary layer. Also a laminar boundary layer has less kinetic energy than a turbulent boundary layer. Therefore the flow in a turbulent boundary layer will be retarded to a lesser degree by an adverse pressure gradient than a turbulent boundary layer. Consequently if transition occurs later the boundary layer is more likely to separate.

A common approach to modelling transitional flows is to set the production terms in the transport equations to zero upstream of the transition location. This requires a priori knowledge of the transition location. Moreover, merely turning on the turbulence model at the transition point does not model the behaviour in the transition region. In the early stages of transition the spectrum of turbulent eddies can not be expected to behave like the typical turbulent energy cascade. Consequently using a universal turbulence model to model the transition region where the flow is atypical is unsuitable. More appropriately we need a separate turbulence model, with different closure coefficients for the transition region.

Wilcox [63] presents a transition model based upon his standard $k-\omega$ model. His transition $k-\omega$ model involves new closures for the k- and ω-equations that are calibrated so that transition is predicted at the correct Reynolds number and has the correct transition length. The model is calibrated to flat plate flow. However since for different flows transition occurs at different Reynolds numbers, this model is not suitable for arbitrary flows. Instead of re-calibrating the model for each new flow, transition can be forced to occur at a pre-specified location. Wilcox triggers transition using a "numerical roughness strip" at the transition point [63]. Roughness is simulated at the transition point by using finite values of ω as the surface boundary condition (see section 9.4). In order to prevent early transition the turbulent kinetic energy must be set at a very small initial value. At the end of the transition region it is necessary to switch to the standard $k-\omega$ model since the transition model is not suitable for the fully turbulent region. The drawback of this method is that the transition location and length must be known a priori.

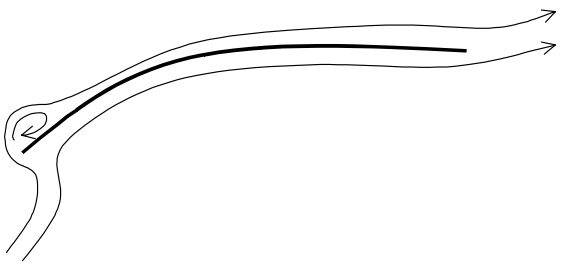

Figure 12: Leading edge separation.

For sail flows it is common for the flow to separate at the leading edge and consequently transition to turbulence occurs in the separation bubble. Therefore it would be suitable to model

the flow over the suction surface of the sail as fully turbulent downstream of the reattachment point. However, how should the separation bubble be treated? Do we model the flow as laminar, turbulent or transitional? It is necessary to perform tests using different models and assess the impact of the various treatments. For many aerofoil flows at Reynolds numbers typical of sail flows the boundary layer remains laminar for a considerable length along the chord on the pressure surface. In fact, at high angles of attack the flow may remain laminar for the entire length of the pressure surface of the aerofoil. For sail flows it is possible that this is also the case. However surface roughness and fittings at the head of the sail are likely to trip transition.

The mainsail presents a different flow situation due to the presence of the mast. IACC masts are long and slender and act as aerofoils when sailing upwind. The flow over the mast is likely to have considerable influence on the flow over the sail. Therefore it may be necessary to model flow transition and investigate the positioning of the transition point on the mast.

10.7 Inlet Turbulence Conditions

In real sailing situations shear between conflicting wind systems and shear generated in the boundary layer above the sea dictate that the onset flow will be turbulent provided the wind speed is at a significant level. Therefore when modelling sail flows it may be suitable to model the entire domain as turbulent flow. However if we model the flow as two-dimensional and set appropriate turbulent inlet conditions then the turbulence will decay, leaving laminar flow upstream of the sails. Since there is little or no stress upstream of the sails to provide energy to the turbulent spectrum the turbulent kinetic energy will be entirely dissipated to thermal energy. In order to simulate real sailing conditions we need to model the three-dimensional effects of the boundary layer above the water surface. That is, source terms need to be included in the turbulent transport equations that model the production of turbulent kinetic energy due to shear stress generated in the vertical direction (the direction we are ignoring in our two-dimensional simulations) in the inlet boundary layer. These terms will need to be calibrated so that turbulent equilibrium is maintained.

10.8 Unsteady Flow

In the high-lift aerodynamic flows computed by Kim et al. [24] it was found that some of their maximum-lift steady state computations did not converge to a steady state. The study was repeated with an unsteady formulation for the flow around the NACA 4412 at an angle of attack of 16°. It was found that the flow was indeed unsteady with periodicity occurring in the lift and drag plots. This was due to the leading-edge laminar separation bubble periodically shedding downstream to the trailing edge. The three models used all gave different lift and drag plots while the average lift and drag values were comparable. The $k-\epsilon$ model predicted no vortex shedding, the $k-\omega$ model predicted dramatic deviations in lift and drag coefficients over a short period and the SST model predicted smaller deviations and a longer period. Unfortunately there was no experimental data to compare the models to. Therefore it is impossible to know which model (if any at all) is predicting the correct behaviour. Moreover it is likely that many downwind sail flows will involve similar unsteady behaviour. Therefore it is necessary to ensure that the turbulence model that is to be used predicts accurate transient behaviour.

In true sailing conditions the onset flow is always unsteady. Therefore to represent real sailing situations the inlet conditions to be used in a computer model should oscillate in both strength and direction. Unsteady inlet conditions are likely to cause unsteady vortex shedding and deviations in lift and drag. Therefore it is important to use an unsteady turbulence model that appropriately models the transient behaviour. Then the unsteady results can be averaged out to present an average flow-field and average lift and drag coefficients.

11 Summary and Model Selection

11.1 Model Summary

The model summaries presented below are broken into the following sections:

Type: Classification of the model, e.g. two-equation, ASM etc.

Designed for: The types of applications the model was developed for.

Wall Boundary Conditions: The treatment of the turbulent parameters at walls.

Strengths: The good features of the model and the flows where it performs particularly well.

Weaknesses: The bad features of the model.

Efficiency Rating: A rating of the model's computational efficiency. 1 to 10, 10 being the best.

Implementation Rating: A rating of the ease of implementation of the model. 1 to 10, 10 being the best.

Suitability for Sail Flows: A conclusion as to how suitable the model is for sail flows.

Type:	Two-equation ($k-\epsilon$) model.
Designed for:	General engineering flows.
Wall boundary conditions:	Wall functions.
Strengths:	1) Efficient since the near wall is not resolved, 2) Numerically stable for most flows.
Weaknesses:	1) Log-law only holds for simple flows, 2) Poor defect layer solutions for adverse pressure gradient flows.
Efficiency rating:	8
Implementation rating:	4, requires the calculation of a wall distance.
Suitability for sail flows:	Unsuitable.

Table 5: The standard $k-\epsilon$ model [23].

Type:	Two-equation ($k-\epsilon$) model.
Designed for:	General engineering flows. Modified from the standard $k-\epsilon$ model to allow integration to solid boundaries.
Wall boundary conditions:	$k=0$, Near-wall behaviour of ϵ is unknown.
Strengths:	Gains average results for a wide range of flows
Weaknesses:	1) Adverse pressure gradients and separating flows, 2) The ϵ-equation can be stiff for wall bounded flows.
Efficiency rating:	4
Implementation rating:	6
Suitability for sail flows:	Unsuitable since adverse pressure gradients and flow separation must be accurately modelled for many sail flows. Likely to perform reasonably well at low-angles of attack.

Table 6: LRN $k-\epsilon$ models [8, 16].

Type:	Two-equation ($k-\omega$) model.
Designed for:	General use. The model can be integrated to the wall without the use of viscous damping functions.
Wall boundary conditions:	$k=0$, $\omega \rightarrow \frac{6\nu}{\beta_o y^2}$, as $y \rightarrow 0$. Finite ω for rough walls.
Strengths:	Excellent results for a wide range of flows, adverse pressure gradients in particular.
Weaknesses:	Dependency on freestream ω values can influence results, especially for free shear flows.
Efficiency rating:	5
Implementation rating:	7
Suitability for sail flows:	Suitable for attached sail flows. May give inaccurate predictions of separation. Freestream dependency a minor problem, but not as serious as for free-shear flows.

Table 7: The standard $k-\omega$ model [60].

Type:	Two-equation ($k-\omega$) model.
Designed for:	General use. Can be integrated to the wall without the use of viscous damping functions. Modified from the standard $k-\omega$ model, removing the model's dependence on freestream ω values.
Wall boundary conditions:	$k=0$, $\omega \rightarrow \frac{6\nu}{\beta_o y^2}$, as $y \rightarrow 0$. Finite ω for rough walls.
Strengths:	Excellent results for a wide range of flows, adverse pressure gradients and free-shear layers in particular.
Weaknesses:	No serious weaknesses apart from its relatively young age. The model needs validation for separated flows.
Efficiency rating:	5
Implementation rating:	6
Suitability for sail flows:	Suitable for attached sail flows, may give inaccurate predictions for separation. Could be modified to give better results for separated flows.

Table 8: The 1998 $k-\omega$ model [67].

Type:	Two-equation ($k-\omega$) model.
Designed for:	Adverse pressure gradient flows and separated flows. Behaves like $k-\omega$ in the near-wall region and like $k-\epsilon$ outside the boundary layer. Designed to remove the freestream dependency of $k-\omega$.
Wall boundary conditions:	$k=0$, $\omega \rightarrow \frac{6\nu}{\beta_o y^2}$, as $y \rightarrow 0$. Finite ω for rough walls.
Strengths:	Excellent results for adverse pressure gradients and separated flows.
Weaknesses:	Not great for free shear flows.
Efficiency rating:	5
Implementation rating:	4, requires the calculation of a wall distance
Suitability for sail flows:	Suitable for both attached and separated sail flows. Needs validation for detached flows past spinnakers.

Table 9: The Shear Stress Transport (SST) model [34, 35].

Type:	Two-equation ($k-\tau$) model.
Designed for:	General use. Similar to LRN $k-\epsilon$ but in terms of τ[s] instead of ϵ.
Wall boundary conditions:	$k=0$, $\tau=0$.
Strengths:	1) Accurately predicts the near-wall asymptotic behaviour for all flow variables, 2) No singularities at solid surfaces.
Weaknesses:	Retains the weaknesses of $k-\epsilon$ models for adverse pressure gradients.
Efficiency rating:	5
Implementation rating:	5
Suitability for sail flows:	As with $k-\epsilon$ models this model is generally unsuitable, however using τ as the second turbulence parameter is attractive.

Table 10: The $k-\tau$ model [56].

Type:	One-equation (ν_T) model.
Designed for:	Aerodynamic flows, adverse pressure gradients, multi-element foils.
Wall boundary conditions:	$\nu_T=0$.
Strengths:	1) Attached aerofoil flows, 2) efficient, 3) very stable, 4) Not bad for small amounts of boundary layer separation.
Weaknesses:	Flows involving jets, large streamline curvature or large amounts of separation and recirculation.
Efficiency rating:	7
Implementation rating:	4, requires the calculation of a wall distance.
Suitability for sail flows:	Model of choice for low angles of attack. Will overpredict separation in high-lift situations.

Table 11: The Spalart-Allmaras model [52].

Type:	Non-linear eddy-viscosity model. Can be used with any two-equation model. We will consider only the $k-\omega$ based model.
Designed for:	Flows where the Reynolds stress tensor may be anisotropic.
Wall boundary conditions:	$k=0$, $\omega \to \frac{6\nu}{\beta_\omega y^2}$, as $y \to 0$. Finite ω for rough walls.
Strengths:	Flows with mild non-equilibrium effects and mild anisotropy.
Weaknesses:	1) Less efficient than two-equation models, 2) There is no evidence that ASM models improve upon the SA and SST models for separated flows, their main advantages are for curved flows and flows in ducts with secondary recirculation.
Efficiency rating:	3
Implementation rating:	5
Suitability for sail flows:	These models may provide improved predictions for highly separated flows and for sails with large curvature. It may be desirable to use an algebraic stress equation in the vortex region downstream of the sails.

Table 12: Explicit Algebraic Stress Models [19, 55].

11.2 Model Suitability for Sail Flows

Turbulence Model	**Model suitability for certain sailing situations (ratings 1-10)**		
	Upwind (Attached)	*Downwind (Separated)*	*Downwind (Stalled)*
Standard $k-\epsilon$	7	2	1
LRN $k-\epsilon$	7	4	3
Standard $k-\omega$	8	6	5
$k-\omega$ *1998*	9	7	6
SST	9	9	8
$k-\tau$	7	4	3
SA	10	6	5
EASM	8	8	9

Table 13: Suitability of turbulence models for different sail flows.

This rating system is an estimate based on material presented in this document. The scores are based predominantly on perceived accuracy, however computational performance and ease of implementation are also considered. As an example, the standard $k-\omega$ always scores one less than the 1998 $k-\omega$ model since it is dependent on freestream values. Also, the ratings have been composed for two-dimensional flows, i.e. the influence of tip vortices has not been considered as at this stage since it is difficult to predict the magnitude of their impact on the results.

11.3 Criteria for Turbulence Model Design

The most important parameter for analysing a sail design is the force prediction. To provide accurate force prediction it is essential that the following features be modelled accurately:

1. The position of separation points.
2. The size and structure of the separation region. In particular we need the surface pressures in the bubble to be accurate as these provide considerable contribution to the overall force.
3. The reformation of boundary layer profiles after reattachment.
4. For three-dimensional flow it is vital that the tip vortices are resolved accurately. Especially in the immediate vicinity of the sail.

11.4 Model Selection

For aerodynamic flows with adverse pressure gradients and possible flow separation the SST model of Menter has been the most accurate performer of the eddy-viscosity models [34, 35]. However Wilcox has eliminated the $k-\omega$ model's dependency on freestream boundary conditions [67]. Therefore there seems to be little need for Menter's cross diffusion term. As an alternative to the SST model, the $k-\omega$ 1998 model could be used with Menter's SST expression for the eddy-viscosity. However this new model would require validation. It is also necessary to investigate the suitability of the ω boundary condition. Possibly a $k-\tau$ formulation would be necessary to avoid the singularity of ω at the wall.

If anisotropic effects are considerable then it may be necessary to use an advanced model. For the large streamline curvature found in downwind sail flows ad hoc curvature corrections to the k- and ϵ-equations may provide some improvement, but would require calibration to experimental data for sail flows. It may be necessary to replace the Boussinesq approximation with an algebraic stress equation. It is hoped that a full second-order closure will not be necessary.

The SA model is more efficient and numerically stable than the ω based models. Therefore it may be useful to implement this model for flows at low angles of attack where it has gained excellent results. It also may be useful to use the SA model to provide an initial solution for a two-equation model.

References

[1] R. Abid. Evaluation of two-equation turbulence models for predicting transition flows. *International Journal of Engineering Sciences*, 31:831–840, 1993.

[2] R. Abid, C. Rumsey, and T. Gatski. Prediction of nonequilibrium turbulent flows with explicit algebraic stress models. *AIAA Journal*, 33(11):2026–2031, 1995.

[3] B. S. Baldwin and T. J. Barth. A one-equation turbulence model for high reynolds number wall bounded flows. Technical Report NASA TM-102847, NASA Lewis Research Centre, 1990.

[4] B. S. Baldwin and H. Lomax. Thin layer approximation and algebraic model for separated turbulent flows. *AIAA Paper 78–257*, 1978.

[5] P. F. Bradshaw, D. H. Ferriss, and N. P. Atwell. Calculation of boundary layer development using the turbulent energy equation. *Journal of Fluid Mechanics*, 28:593–616, 1967.

[6] T. Cebici and A. M. O. Smith. *Analysis of Turbulent Boundary Layers*. Series in Applied Mathematics and Mechanics. Academic Press, Orlando, FL, 1974.

[7] H. C. Chen and V. C. Patel. Near-wall turbulence models for complex flows including separation. *AIAA Journal*, 26(6):641–648, 1988.

[8] K.-Y. Chien. Prediction of channel and boundary-layer flows with a low-reynolds-number turbulence model. *AIAA Journal*, 20(1):33–38, 1982.

[9] D. Coles and A. J. Wadcock. Flying-hot-wire study of flow past an naca 4412 airfoil at maximum lift. *AIAA Journal*, 17(4):321–329, 1979.

[10] D. E. Coles and Hirst E. A. Computation of turbulent boundary layers-1968 AFSOR-IFP-stanford conference, vol II. Thermosciences Division, Stanford University, CA, 1969.

[11] S. J. Collie. Numerical modelling of the three-dimensional turbulent flow over yacht sails. Master's thesis, Department of Engineering Science, University of Auckland, 2000.

[12] S. J. Collie and M. Gerritsen. Modelling sail flows using fluent. *Journal of Wind Engineering and Industrial Aerodynamics*, 2001. Yet to be published.

[13] T. J. Craft, B. E. Launder, and K. Suga. Extending the applicability of eddy viscosity models through the use of deformation invariants and non-linear elements. In *Refined Flow Modelling and Turbulence Measurements - 5th International Symposium*, pages 125–132, Paris, 1996.

[14] T. J. Craft, B. E. Launder, and K. Suga. Development and application of a cubic eddy-viscosity model of turbulence. *Interenational Journal of Heat and Fluid Flow*, 17(2):108–115, 1997.

[15] D. M. Driver. Reynolds shear stress measurements in a separated boundary layer. Technical Report AIAA Paper, 91-1787, 1991.

[16] Launder B. E. and Sharma B. I. Application of the energy-dissipation model of turbulence to the calculation of flow near a spinning disk. *Letters in Heat and Mass Transfer*, 1:131–138, 1974.

[17] J. H. Ferziger. *Recent Advances in Large-Eddy Simulation, Engineering Turbulence Modelling and Experiments 3 (W. Rodi and G. Begeles, eds.)*. Elsever, 1996.

[18] S.P. Fiddes and J. H. Gaydon. A new vortex–lattice method for calculating the flow past yacht sails. *Journal of Wind Engineering and Industrial Aerodynamics*, 63:35–59, 1996.

[19] T. B. Gatski and C. G. Speziale. On explicit algebraic stress models for complex turbulent flows. *Journal of Fluid Mechanics*, 254:59–78, 1993.

[20] P. Godin, D. W. Zingg, and T. E. Nelson. High–lift aerodynamic computations with one– and two– equation turbulence models. *AIAA Journal*, 38(2):237–243, 1997.

[21] D. A. Johnson and T. J. Coakley. Improvements to a nonequilibrium algebraic turbulence model. *AIAA Journal*, 26(11):2000–2003, 1990.

[22] D. A. Johnson and L. S. King. A mathematically simple turbulence closure model for attached and separated turbulent boundary layers. *AIAA Journal*, 23(11):1684–1692, 1985.

[23] W. P. Jones and B. E. Launder. Prediction of laminarization with a two-equation model of turbulence. *International Journal of Heat and Mass Transfer*, 15:301–314, 1972.

[24] S.-E. Kim and D. Choudhury. A near–wall treatment using wall functions sensitized to pressure gradient. *AMSE FED Separated and Complex Flows*, 217, 1995.

[25] A. N. Kolmogorov. Equations of turbulent motion of an incompressible fluid. Technical Report 1–2, Izvestia Academy of Sciences, USSR; Physics, 1942.

[26] C. K. G. Lam and K. A Bremhorst. Modified form of $k - \epsilon$ model for predicting wall turbulence. *Journal of Fluids Engineering, Transactions of the ASME*, A317:415–433, 1981.

[27] B. E. Launder and N. Shima. Second-moment closure for the near-wall sublayer: Development and application. *AIAA Journal*, 27(10):1319–1325, 1989.

[28] J. L. Lumley. Computational modelling of turbulent flows. *Advances in Applied Mechanics*, 18:123–176, 1978.

[29] F. R. Menter. Influence of freestream values on $k - \omega$ turbulence model predictions. *AIAA Journal*, 30(6):1657–1659, 1992.

[30] F. R. Menter. Performance of popular turbulence models for attached and separated adverse pressure gradient flows. *AIAA Journal*, 30(8):2066–2072, 1992.

[31] F. R. Menter. Comparison of some recent eddy-viscosity turbulence models. *Journal of Fluids Engineering, Transactions of the ASME*, 118:514–519, 1996.

[32] F. R. Menter. Eddy viscosity transport equations and their relation to the $k - \epsilon$ model. *Journal of Fluids Engineering-Transactions of the ASME*, 118(3):876–884, 1997.

[33] F.R. Menter. Improved two-equation $k - \omega$ turbulence models for aerodynamic flows. Technical Report TM-103975, NASA, 1992.

[34] F.R. Menter. Zonal two-equation $k - \omega$ turbulence models for aerodynamic flows. Technical Report AIAA Paper 93-2906, AIAA, 1993.

[35] F.R. Menter. Two–equation eddy–viscosity turbulence models for engineering applications. *AIAA Jounal*, 32(8):1598–1605, 1994.

[36] P. Moin and K. Mahesh. Direct numerical simulation: A tool in turbulence research. *Annual Review of Fluid Mechanics*, 30:539–578, 1998.

[37] V. C. Chon Patel, J. T., and Yoon J. Y. Turbulent flow in a channel with a wavy wall. *ASME Journal of Fluids Engineering*, 113:579–586, 1991.

[38] S. H. Peng, Davidson L., and Holmberg S. A modified low-reynolds-number $k - \omega$ model for recirculating flows. *Journal of Fluids Engineering, Transactions of the ASME*, 119:867–875, 1997.

[39] L. Prandtl. Uber die ausgebildete turbulenz. *ZAMM*, 5:136–139, 1925.

[40] L. Prandtl. Uber ein neues formelsystem fur die ausgebildete turbulenz. *Gottingen, Math-Phys. Kl*, pages 301–314, 1945.

[41] O. Reynolds. An experimental investigation of the circumstances whcih determine whether the motion of water shall be direct or sinuous, and of the law of resistance in parallel channels. *Royal Society Phil. Trans.*, 1883.

[42] D. F. Robinson, J. E. Harris, and H. A. Hassan. Unified turbulence closure model for axisymmetric and planar free shear flows. *AIAA Journal*, 33(12):2325–2231, 1995.

[43] W. Rodi. Comparison of LES and RANS calculations of the flow around bluff bodies. *Journal of Wind Engineering and Industrial Aerodynamics*, 69–71:55–75, 1997.

[44] W. Rodi. Large-eddy simulations of the flow past bluff bodies - state-of-the-art. *Japan Society of Mechanical Engineers International Journal, Series B*, 41(2):1–53, 1998.

[45] C. L. Rumsey, T. B. Gatski, and J. H. Morrison. Turbulence model predictions of strongly curved flow in a u-duct. *AIAA Journal*, 38(8):1394–1402, 2000.

[46] C. L. Rumsey, T. B. Gatski, Ying S. X., and Bertelrud A. Evaluation of two-equation turbulence models for predicting transition flows. *AIAA Journal*, 36(5):765–774, 1998.

[47] P. G. Saffman. A model for inhomogeneous turbulent flow. *Proceedings of the Royal Society, London*, 1970.

[48] H. Schlichting. *Boundary Layer Theory, Seventh Ed.* McGraw-Hill, New York, NY, 1997.

[49] W. H. Schofield. Two–dimensional separating turbulent boundary layers. *AIAA Journal*, 21(10):1611–1620, 1986.

[50] T. H. Shih, W. W. Liou, A. Shabbir, and J. Zhu. A new k- eddy-viscosity model for high reynolds number turbulent flows - model development and validation. *Compuers and Fluids*, 24(3):277–238, 1995.

[51] R. M. C. So and G. L. Mellor. Turbulent boundary layers with with large streamline curvature effects. Technical Report CR-1940, NASA, 1972.

[52] P. R. Spalart and S. R. Allmaras. A one–equation turbulence model for aerodynamics flows", journal="la recherche aerospatiale. (1):5–21, 1994.

[53] C. G. Speziale. On nonlinear $k-l$ and $k-\epsilon$ models of turbulence. *Journal of Fluid Mechanics*, 178:459–475, 1987.

[54] C. G. Speziale. Analytical methods for the development of reynolds-stress closures in turbulence. *Annual Review of Fluid Mechanics*, pages 107–157", 1991.

[55] C. G. Speziale. Comparison of explicit and traditional algebraic stress models of turbulence. *AIAA Journal*, 35(9):1506–1509, 1997.

[56] C. G. Speziale, R. Abid, and E. C. Anderson. Critical evaluation of two-equation models for near-wall turbulence. *AIAA Journal*, 30(2):324–331, 1992.

[57] M. Strelets. Detached eddy simulation of massively separated flows. *AIAA Paper 2001–0879*, 2001.

[58] S. U. Svennberg. *On Turbulence Modelling for Bilge Vortices: A Test of Eight Models for Three Cases.* PhD thesis, Department of Naval Architecture and Ocean Engineering, Chalmers University of Technology, Göteborg, Sweden, 2001.

[59] A. A. Townsend. Equilibrium layers and wall turbulence. *Journal of Fluid Mechanics*, 11, 1962.

[60] D. C. Wilcox. Reassessment of the scale-determining equation for advanced turbulence models. *AIAA Journal*, 26(11):1299–1310, 1988.

[61] D. C. Wilcox. A half century historical review of the $k-\omega$ model. Technical Report AIAA paper 91–0615, AIAA, 1991.

[62] D. C. Wilcox. *Turbulence Modelling for CFD, 1st Edition*. Griffin Printing, California., 1993.

[63] D. C. Wilcox. Simulation of transition with a two-equation turbulence model. *AIAA Journal*, 32(2):247–255, 1994.

[64] D. C. Wilcox and T. L. Chambers. Further refinement of the turbulence model transition prediction technique. Technical Report DCW-R-03-02, DCW Industries, La Canada, CA, 1975.

[65] D. C. Wilcox and T. L. Chambers. Streamline curvature effects on turbulent boundary layers. *AIAA Journal*, 15(4):574–580, 1977.

[66] D. C. Wilcox and M. W. Rubesin. Progress in turbulence modelling for complex flow fields including effects of compressibility. Technical Report NASA TP–1517, 1980.

[67] D.C. Wilcox. *Turbulence Modeling for CFD, 2nd Edition*. Griffin Printing, California, 1998.

[68] V. Yakhot and S. Orszag. Renormalization group analysis of turbulence. *Journal of Scientific Computing*, 1, 1986.

[69] S. L. Yang, Y. L. Chang, and O. Arici. Navier–stokes computations of the nrel airfoil using a $k-\omega$ turbulent model at high angles of attack. *Journal of Solar Energy Engineering, Transactions of the ASME*, 117:304–310, 1995.